Shallow structure of the Cascadia subduction zone beneath western Washington from spectral ambient noise correlation

Josh A. Calkins,[1] Geoffrey A. Abers,[1] Göran Ekström,[1] Kenneth C. Creager,[2] and Stéphane Rondenay[3]

Received 20 April 2010; revised 15 March 2011; accepted 6 April 2011; published 12 July 2011.

[1] High-resolution 3-D shear velocity (Vs) images of the western Washington lithosphere reveal structural segmentation above and below the plate interface correlating with transient deformation patterns. Using a spectral technique, phase velocities are extracted from cross-correlated ambient noise recorded by the densely spaced "CAFE" broadband array. The spectral approach resolves shear velocities at station offsets less than 1 wavelength, significantly shorter than typically obtained by standard group velocity approaches, increasing the number of useable paths and resolution. Tomographic images clearly illuminate the high Vs (>4.5 km/s) subducting slab mantle. The most prominent anomaly is a zone of low Vs (3.0–3.3 km/s) in the middle to lower continental crust, directly above the portion of the slab expected to be undergoing dehydration reactions. This low-velocity zone (LVZ), which is most pronounced beneath the Olympic Peninsula, covers an area both spatially coincident with and updip of the region of most intense episodic tremor and slip (ETS). The low Vs and comparison with published P wave velocity models indicate that Vp/Vs ratios in this region are greater than 1.9, suggesting a fluid-rich lower crust. The LVZ disappears southward, near 47°N, coincident with sharp decreases in intraslab seismicity and ETS activity as well as structural changes in the slab. The spatial coincidence of these features suggests that either underthrusting of hydrated low-velocity material or long-term fluid fluxing of the overriding plate via dewatering of a persistently hydrated patch of the Juan de Fuca slab may partially control slip on the plate interface and impact the rheology of the overriding continental crust.

Citation: Calkins, J. A., G. A. Abers, G. Ekström, K. C. Creager, and S. Rondenay (2011), Shallow structure of the Cascadia subduction zone beneath western Washington from spectral ambient noise correlation, *J. Geophys. Res.*, *116*, B07302, doi:10.1029/2010JB007657.

1. Introduction

[2] It is often hypothesized that long-lived geologic structures limit the rupture extent of large subduction zone thrust earthquakes [e.g., *Kelleher and McCann*, 1976; *Jordan et al.*, 1983; *Wells et al.*, 2003; *Fuller et al.*, 2006]. While this hypothesis has been difficult to test due to the long repeat times of great megathrust earthquakes, there have been some clear cases where bathymetric features in the downgoing plate or structural features within the overriding plate coincide closely with the limits or segmentation of rupture [e.g., *DeShon et al.*, 2003]. Recently discovered aseismic creep events, slow earthquakes, and accompanying tremor [e.g., *Rogers and Dragert*, 2003], loosely termed Episodic Tremor and Slip (ETS), show a different mode of plate boundary deformation that also occurs in spatially limited and repeating patches along strike. Most ETS events arise downdip (and perhaps updip) from the locked zone of regular earthquakes, and fluids have been postulated to play a critical role in their occurrence [e.g., *Kao et al.*, 2005; *Liu and Rice*, 2007]. Hence, the occurrence of ETS may be also controlled by plate structure, albeit in a manner different from megathrust earthquakes. For example, ETS events may be localized to zones of high permeability or pore pressure.

[3] The subduction interface beneath Western Washington hosts one of the first recognized and most reliably episodic zones of ETS [e.g., *Miller et al.*, 2002; *Dragert et al.*, 2004]. It continues to be among the best studied, with a record of regular slip and tremor occurrence longer than a decade in the northern part [e.g., *Wech et al.*, 2010; *Kao et al.*, 2009], and a several year record of tremor along the length of the margin [*Brudzinski and Allen*, 2007]. Tremor here seems to

[1]Lamont-Doherty Earth Observatory, Earth Institute at Columbia University, Palisades, New York, USA.
[2]Department of Earth and Space Science, University of Washington, Seattle, Washington, USA.
[3]Department of Earth, Atmospheric, and Planetary Sciences, Massachusetts Institute of Technology, Cambridge, Massachusetts, USA.

0148-0227/11/2010JB007657

be segmented along strike, with segment boundaries corresponding to other long-term segmentation of the margin, for example in intraslab seismicity. However, it is less clear how this segmentation corresponds to structural variations near the plate interface, where presumably variations in material properties have the most control over ETS generation.

[4] In this paper, we present the first shear wave images of the Cascadia subduction zone to evaluate these variations in material properties. The images are derived from ambient noise tomography (ANT), a recently developed technique that provides a powerful tool for investigating earth structure at middle and lower crustal depths, precisely the depths where the plate boundary lies in the region of ETS generation. Our models constrain the shear velocity structure in the region where ETS signals originate, and shed light on the possible linkages with fluids released as a by-product of subduction. The tomographic images show strong variations in overriding plate structure that appear generated by long-lived spatial variations in dehydration of the downgoing plate; the strongest variations correspond closely to the first-order segmentation of ETS.

2. Tectonic Setting

[5] Cascadia has produced very few instrumentally recorded thrust zone earthquakes [*Tréhu et al.*, 2008], although paleoseismic and geodetic evidence indicates that great earthquakes can occur [*Atwater*, 1987; *Hyndman and Wang*, 1995]. Both the overriding and subducting plates are seismically active in northern and central Washington. Intraslab seismicity decreases drastically south of 47°N [*McCrory et al.*, 2004]. The thermal and petrologic conditions that contribute to this particular behavior along the Cascadia megathrust have been the subject of intense geophysical study in recent years, however interpretations of seismic data have been limited by the lack of information on plate structure in the crust and upper mantle of the overriding North American plate. P wave tomography studies using local earthquakes [e.g., *Lees and Crosson*, 1990; *Moran et al.*, 1999], reflection and refraction data [e.g., *Parsons et al.*, 1998] or simultaneous inversions of both [*Parsons et al.*, 1999; *Van Wagoner et al.*, 2002; *Preston et al.*, 2003; *Ramachandran et al.*, 2006; *Calvert et al.*, 2006] have produced high-fidelity images of the P wave velocities across much of Cascadia, and receiver function migration studies [e.g., *Rondenay et al.*, 2001; *Nicholson et al.*, 2005; *Nikulin et al.*, 2009; *Abers et al.*, 2009] have mapped the seismic discontinuity structure along several trench-perpendicular transects. Both techniques, however, are restricted to resolving structure along the raypaths sampled by seismic waves between the limited sources and receivers available to each study. Furthermore, the lack of shear velocity information for Cascadia hampers interpretations of overriding plate lithology.

[6] The overriding plate in Western Washington is comprised of accretionary wedge rocks that have been smeared into a host assemblage of accreted terranes grading eastward into the Tertiary and Quaternary Cascade arc [e.g., *Parsons et al.*, 1999]. The largest of the accreted terranes in the vicinity of our study area is the Crescent Terrane, a largely basaltic and gabbroic oceanic terrane whose accretion between 50 and 45 Ma likely caused the trench to jump oceanward by ~200 km [*Madsen et al.*, 2006]. Southward, the Crescent Terrane has equivalent lithology and similar origin to the Siletz Terrane [e.g., *Parsons et al.*, 1998]. The Crescent Terrane is seismically faster than the surrounding host rock and has been mapped to 25 km depth beneath Puget Sound [*Ramachandran et al.*, 2006]. *Parsons et al.* [1999] suggest that the high rigidity of the Crescent Terrane compared to the surrounding older accreted terranes, accretionary wedge materials, and Cascade volcanics, may lead to focusing of deformation and overriding plate earthquakes along its margins.

[7] The Juan de Fuca plate subducts beneath North America at a rate of 35–41 mm/yr at an azimuth of 55–63° [*DeMets and Dixon*, 1999; *Wilson*, 2002] and the plate is only ~10 My old at the trench [*Wilson*, 2002]. There have been no large megathrust earthquakes during historic times, but geologic evidence indicates that earthquakes with magnitudes of 8.0 or larger occur with recurrence intervals of hundreds of year [e.g., *Atwater*, 1992; *Satake et al.*, 2003; *Goldfinger et al.*, 2003]. The most damaging historical earthquakes in the region are intermediate depth intraslab events, with the most recent being the Mw 6.8 Nisqually earthquake (Figure 1), which occurred at a depth of 50–60 km beneath southern Puget Sound in 2001 [e.g., *Bustin et al.*, 2004]. Slab earthquakes terminate south of approximately 47°N and are almost entirely absent from central Washington to northern California [*McCrory et al.*, 2004].

[8] Between the locked zone offshore and the (presumably) freely slipping zone at depth, some combination of the thermal and rheological properties of the plate interface allows it to slip during distinct, slow events on a roughly 14 month interval [e.g., *Miller et al.*, 2002; *Rogers and Dragert*, 2003]. These geodetically observed slip events are accompanied by low frequency tremors that have been variously located at [e.g., *Wech and Creager*, 2008; *La Rocca et al.*, 2009; *Brown et al.*, 2009] or above [e.g., *McCausland et al.*, 2005; *Kao et al.*, 2009] the plate interface. Inversions of the geodetic signal indicate that between 8% [*McCaffrey*, 2009] and 65% [*Wech et al.*, 2010] of the interplate convergence is accommodated during the regular 14 month ETS events, and perhaps more strain is released during smaller slip events between the main ETS episodes [*Wech et al.*, 2010].

3. Data and Methods

3.1. Noise Correlation

[9] Our data set consists of 24 months of continuous vertical component broadband data recorded by the Cascadia Arrays for Earthscope (CAFE) project [*Abers et al.*, 2009], supplemented with data from nearby EarthScope Transportable Array (TA) stations. Station density varies, with the densest coverage (~5–20 km spacing) along an E-W striking line near 47°N (Figure 1). Coverage is sparser northeast of Seattle and on the Olympic Peninsula, where the minimum interstation distances approach 80 km. The 64 stations shown in Figure 1 yield over 1900 useable paths and dense ray coverage over much of western Washington (Figure 2).

[10] We prepare the waveforms for cross correlation in a manner similar to the best practices prescribed by *Bensen et al.* [2007], using routines adapted from those developed by

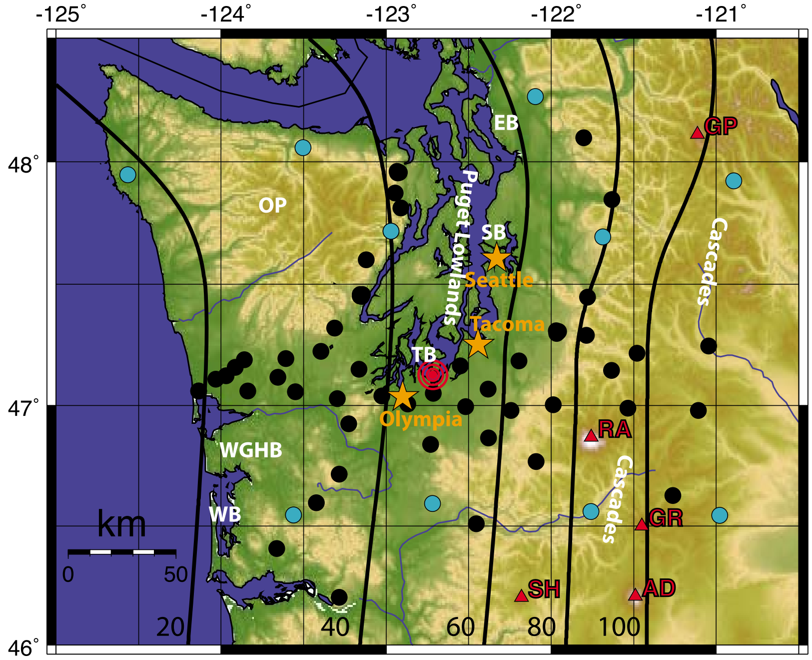

Figure 1. Map of study area showing locations of CAFE (black circles) and EarthScope Transportable Array (blue circles) stations used in the ambient noise tomography. Also shown are depth contours to the top of the slab (black lines and numbers) [after *McCrory et al.*, 2004], major Cascade volcanoes (red triangles), and selected cities (orange stars and labels). The red circles NE of Olympia mark the epicenter of the 2001 Mw 6.8 Nisqually earthquake [*Bustin et al.*, 2004]. AD, Mount Adams; EB, Everett Basin; GP, Glacier Peak; GR, Goat Rocks; OP, Olympic Peninsula; RA, Mount Rainier; SB, Seattle Basin; SH, Mount St. Helens; TB, Tacoma Basin; WB, Willapa Bay; WGHB, Willapa-Grays Harbor Basin.

Stachnik et al. [2008]. After applying a zero-phase FIR antialias filter with 0.4 Hz corner, the raw data are decimated to 1 sample per second from the original 40 (CAFE) or 50 (TA) sample per second streams, windowed to hour long segments, and detrended. We then remove the instrument response, whiten the spectrum by dividing the complex frequency by its magnitude, taper the time domain signal, and apply a five-pole Butterworth filter with a passband of 0.003–0.3 Hz. We partially mitigate the dominance of high amplitude transient signals (e.g., earthquakes) by normalizing each hour long window by its envelope. This approach, combined with the effect of cross correlating and stacking relatively short (10 min) data windows, suppresses earthquake signals as effectively as one-bit normalization without

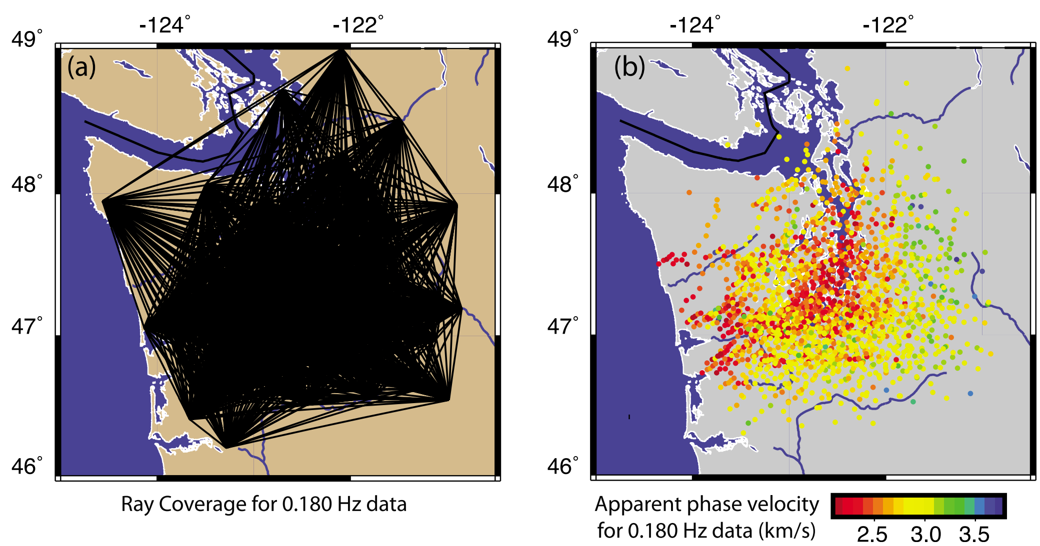

Figure 2. Example intermediate processing results for the 0.180 Hz data set. (a) Paths showing NCF ray coverage. (b) Colored circles reflect the apparent phase velocity for a NCF between two stations and are plotted at the midpoint of the path connecting the station pair.

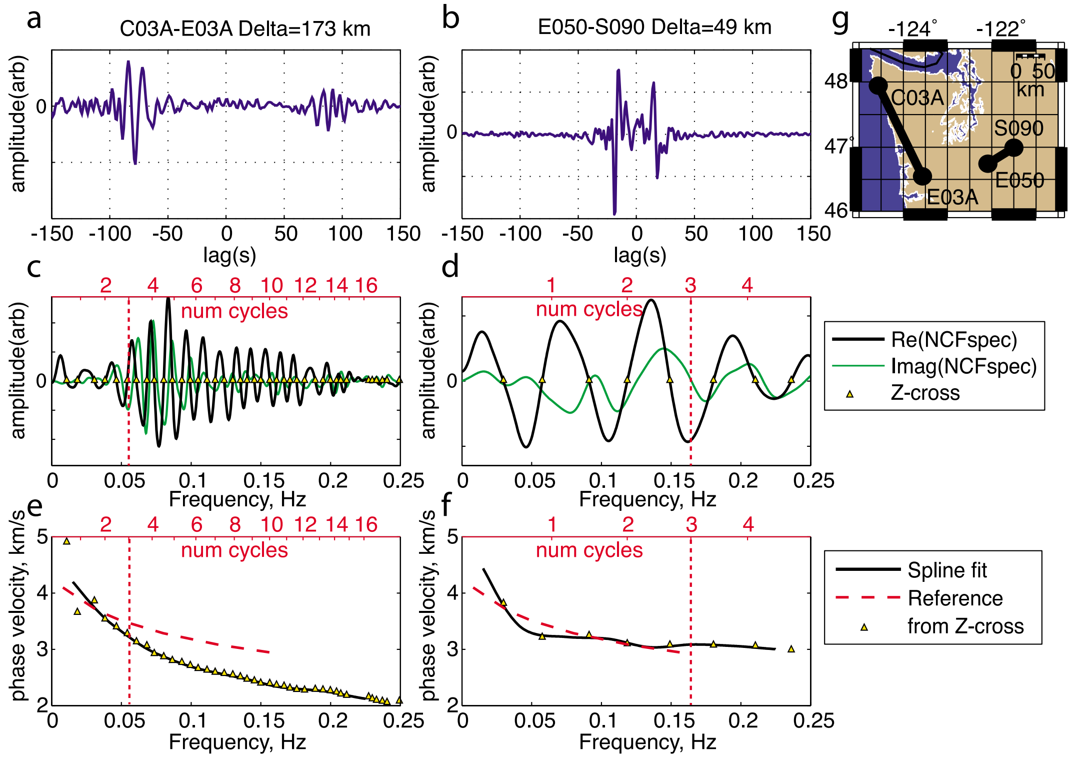

Figure 3. Examples of phase velocity estimation in the frequency domain. (a–b) Time domain Noise Correlation Functions (NCFs) for station pairs separated by 173 and 49 km, respectively. (c–d) The real (black line) and imaginary (green line) parts of the NCF spectra are plotted for the same station pairs, along with the zero crossings of the real part (yellow triangles). (e–f) Phase velocities derived from the zero crossings using equation (2). The vertical red dashed lines in Figures 3c–3f mark the 3λ cutoff imposed by most time domain ambient noise studies. The red dashed curve in Figures 3e–3f is a reference dispersion curve from a tectonically analogous region from *Harmon et al.* [2008]. (g) Map showing station locations and paths.

modifying the signal as aggressively, thereby increasing the ability to recover stable results even for low-amplitude cross correlations.

[11] After preprocessing, the 1 h segments are cut into 10 min windows and cross correlated for all possible station pairs. The resulting noise correlation functions (NCFs) are normalized to unit amplitude and averaged for each interstation path. A signal-to-noise ratio is constructed by dividing the maximum amplitude of the NCF within a window around the predicted maximum signal by the RMS amplitude within a window centered at 200 s lag, well beyond the time expected to contain the signal of interest. NCFs with a signal-to-noise ratio of less than 20 are discarded, reducing our overall data set by less than 2%. We also discard data from any interstation paths shorter than 40% of the expected wavelength at the period of interest (as explained below). Finally, we cull outliers, which we define as phase velocity measurements greater than 2.5 standard deviations from the mean observed phase velocity at a given period for the entire data set.

3.2. Phase Velocity Measurements and Inversions

[12] The usual path from noise correlation function (NCF) to velocity model involves estimating group velocity (often employing frequency-time analysis) [e.g., *Shapiro and Campillo*, 2004; *Sabra et al.*, 2005; *Moschetti et al.*, 2007; *Lin et al.*, 2007], followed by inversions for phase and/or shear velocity [e.g., *Harmon et al.*, 2007; *Stachnik et al.*, 2008]. Implicit in this approach is the assumption that the NCFs approximate the Green functions for the path between a given receiver pair [e.g., *Sanchez-Sesma and Campillo*, 2006]. This approach to extracting velocities from NCFs, however, is limited to station pair paths that are at least 2 [e.g., *Shapiro et al.*, 2005] or 3 times [e.g., *Lin et al.*, 2008] longer than the dominant wavelength being measured, due in part to interference between precursors to the arrivals at positive and negative lags [e.g., *Lin et al.*, 2007; *Bensen et al.*, 2007]. Instead, we apply a frequency domain technique based on *Ekström et al.* [2009] to measure phase velocities from NCFs, which allows the inclusion of much shorter paths (or longer wavelengths for a given station spacing). For clarity, we describe each of the three processing steps individually and assess uncertainty associated with each step.

3.2.1. Step 1: Phase Velocity Measurement

[13] *Aki* [1957] shows that the azimuthally averaged spectral correlation function for 2 stations, $\rho(r, \omega_o)$, is related to the phase velocity by the relationship

$$\rho(r, \omega_0) = J_0\left(\frac{\omega_0}{c(\omega_0)} r\right) \quad (1)$$

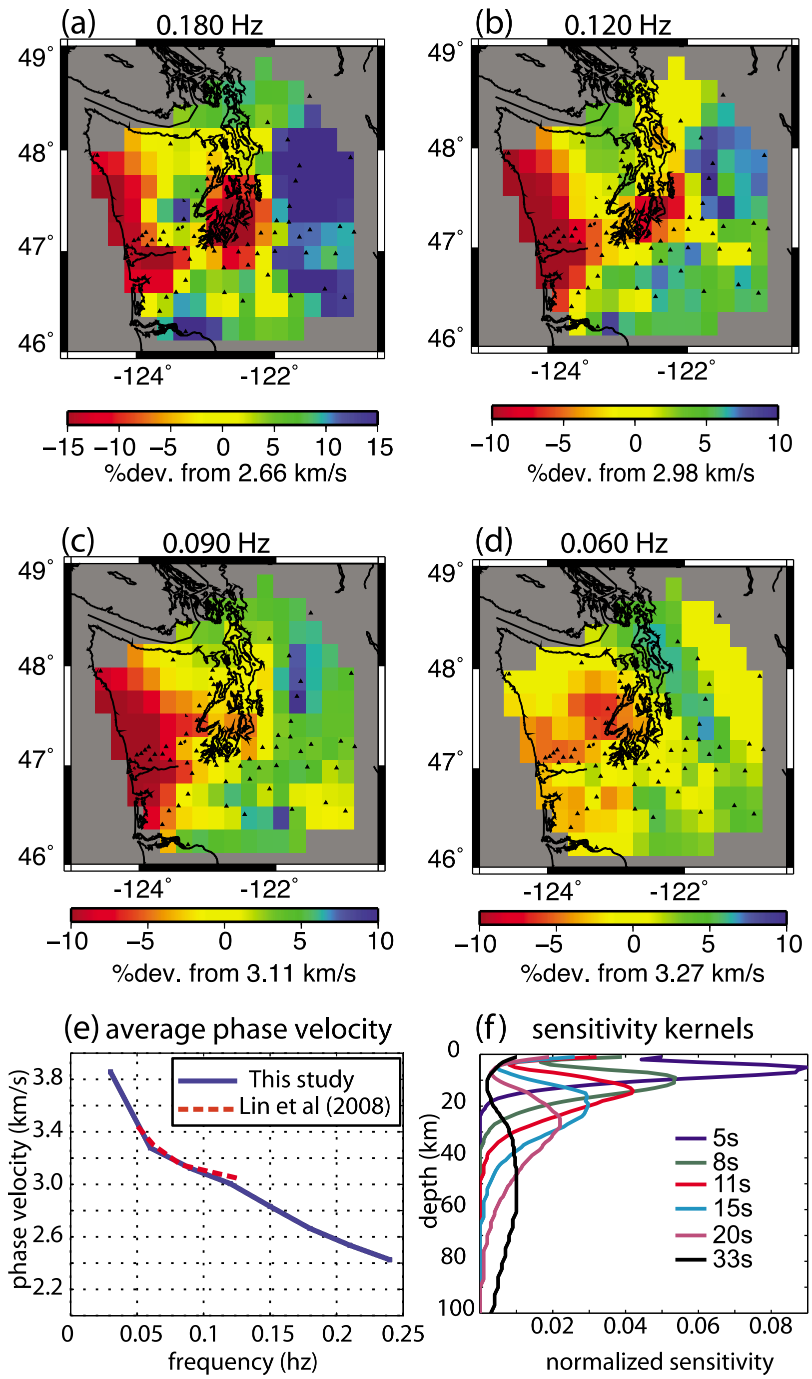

Figure 4. Phase velocity models and sensitivity kernels. (a–d) Selected phase velocity maps on a 0.25° × .25° grid. Small black triangles mark station locations. Frequency and average phase velocity are indicated at the top and bottom of each map, respectively. Gray areas are regions with no interstation phase velocity estimates. (e) Comparison the average phase velocities from this study with those reported for the western United States by *Lin et al.* [2008]. (f) Curves are normalized Rayleigh wave sensitivity kernels for the starting model used in the shear velocity inversions.

where r is the interstation distance, $c(\omega_o)$ is the phase velocity at angular frequency ω_o, and J_0 is the zeroth order Bessel function of the first kind. This relationship forms the basis for our phase velocity estimations (for more details on this approach, see *Ekström et al.* [2009]). The spectral amplitude, however, is partially controlled by the (unknown) spectrum of the ambient noise field and the nonlinear effects associated with preprocessing. Thus, rather than attempting to match the cross spectrum directly, we solve for $c(\omega_n)$ by equating the zero crossings of the real part of the spectrum of

Table 1. 1-D Starting Model as Input Into Surf96[a]

Top of Layer	Layer Thickness	Vp	Vs	Density
0	4	5.4	3.09	2.6
4	4	6.38	3.65	2.6
8	4	6.59	3.77	2.8
16	4	6.59	3.77	2.8
20	4	6.73	3.85	3.1
24	5	6.86	3.92	3.1
29	4	6.96	3.98	3.1
33	4	7.20	4.115	3.2
37	4	7.40	4.229	3.3
41	10	7.60	4.343	3.4
51	10	7.80	4.46	3.5
61	10	7.80	4.46	3.5
71	10	7.80	4.46	3.5
81	10	7.80	4.46	3.5
91	10	7.80	4.46	3.5
101	half-space	7.80	4.46	3.5

[a]Vp values are roughly based on the work of *Ludwin et al.* [1991] and *Abers et al.* [2009], with a gradient introduced between 29 km and 51 km to allow the inversion to accommodate varying Moho depths across the model.

the NCFs with the zero crossings, z_n, of the J_0 Bessel function:

$$c(\omega_n) = \frac{\omega_n r}{z_n} \tag{2}$$

where we approximate z_n using a McMahon's series expansion [*Abramowitz and Stegun*, 1965, equation 9.5.12]. The imaginary part of the spectrum is zero if the distribution of noise sources is azimuthally uniform, and remains small for modest, low-order azimuthal noise variations [*Cox*, 1973; *Webb*, 1986]. Large nonzero imaginary components, therefore, are indicative of significant azimuthal variations in the power of the noise.

[14] We select phase velocities at observed zero crossings in a manner similar to that described by *Ekström et al.* [2009], and fit a cubic hermite spline to interpolate the $c(\omega_n)$ to uniform frequency sampling at 0.03 Hz intervals via a damped least squares inversion (Figure 3). The spline is fit to the data points in a least squares sense, and formal uncertainties in the least squares fitting are used to weight the observations in the subsequent tomographic inversion.

3.2.2. Step 2: Phase Velocity Regularization

[15] The individual path NCFs are then inverted to create 2-D phase velocity maps. At each of 8 frequencies ranging from 0.03 to 0.24 Hz, we use the path-averaged phase velocity observations to invert for a smooth phase velocity model on a 0.25° × 0.25° grid (Figure 4). A small amount of damping is applied to the inversion to minimize model roughness.

3.2.3. Step 3: Shear Velocity Inversion

[16] At each grid node, dispersion curves are extracted and inverted via an iterative, linearized least squares routine (*surf96*) [*Herrmann and Ammon*, 2004] for 1-D Vs profiles. We use a one-dimensional starting model adapted from *Ludwin et al.* [1991] and *Abers et al.* [2009] to include a gradual transition from lower crustal velocities at 29 km depth to upper mantle velocities at 51 km (Table 1). To stabilize the inversions at longer periods, we add phase velocity constraints from observations of ballistic surface waves at periods of 40, 50, and 66 s prior to inverting for shear velocity.

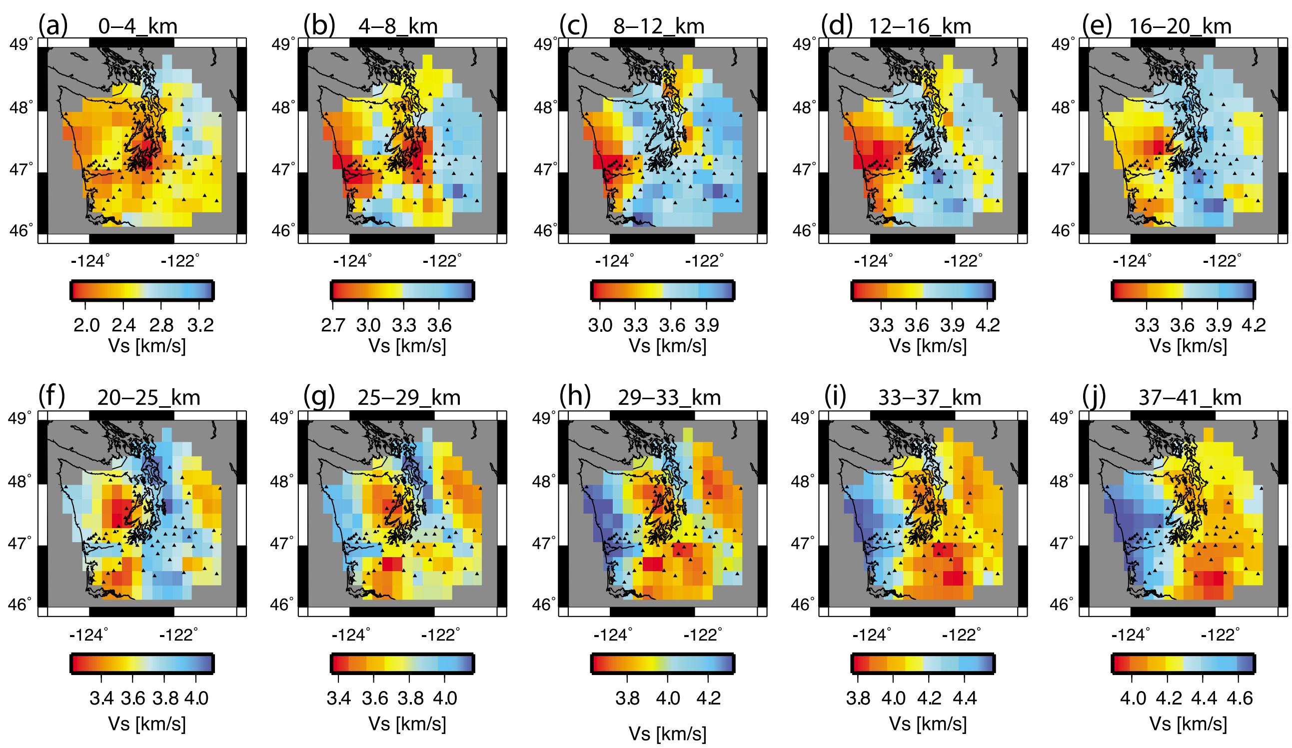

Figure 5. Shear velocity maps resulting from 1-D inversion of phase velocities at evenly spaced points separated by 0.25°. Depth and Vs scale are indicated at the top and bottom of each map, respectively.

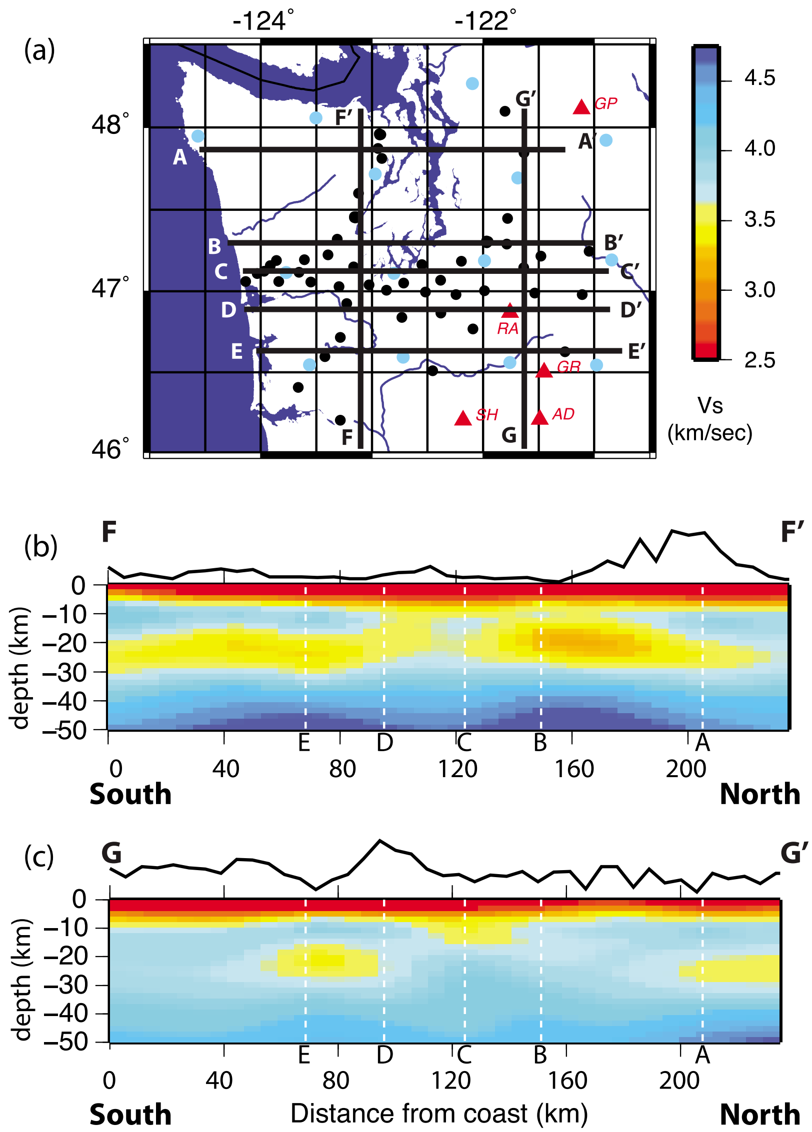

Figure 6. (a) Reference map and (b–c) south-north oriented cross sections through the final shear velocity model. Black lines and labels on the map indicate the position of cross sections F-F′ and G-G′ here, as well as the locations of the cross sections in Figures 7, 8, and 14. Other symbols on the map are the same as in Figure 1. Topographic profiles above each cross section have 10:1 vertical exaggeration. White dashed lines and labels on the *x* axis in Figures 6b and 6c mark the locations where the west-east oriented cross sections (Figure 7) intersect.

These data come from previously published results based on EarthScope Transportable Array data [*Yang et al.*, 2008] and were interpolated to our quarter-degree grid. The inversion is run iteratively, following the approach detailed by *Larson et al.* [2006] and *Warren et al.* [2008], with the damping parameter decreased between successive iterations to the point where the decrease in misfit is minimal and 1-D shear velocity profiles become unrealistically oscillatory. Because several body wave tomography studies [e.g., *Ramachandran et al.*, 2006; *Preston*, 2003; *Parsons et al.*, 1999] and a recent regional-scale ambient noise tomography study [*Moschetti et al.*, 2010] have shown that low-velocity zones are prevalent in the lower crust of the Cascades, we choose to allow the inversion to include layers in which Vs decreases with depth.

4. Results

4.1. Phase Velocity

[17] Phase and shear velocity maps as well as cross sections through the final Vs model are presented in Figures 4–7. The phase velocity maps largely reflect the shallow structure, particularly at the higher frequencies (Figures 4a and 4b). The Seattle Basin and the accretionary wedge rocks of the Olympic Peninsula are prominent low-velocity features at frequencies greater than 0.10 Hz. Slightly higher phase

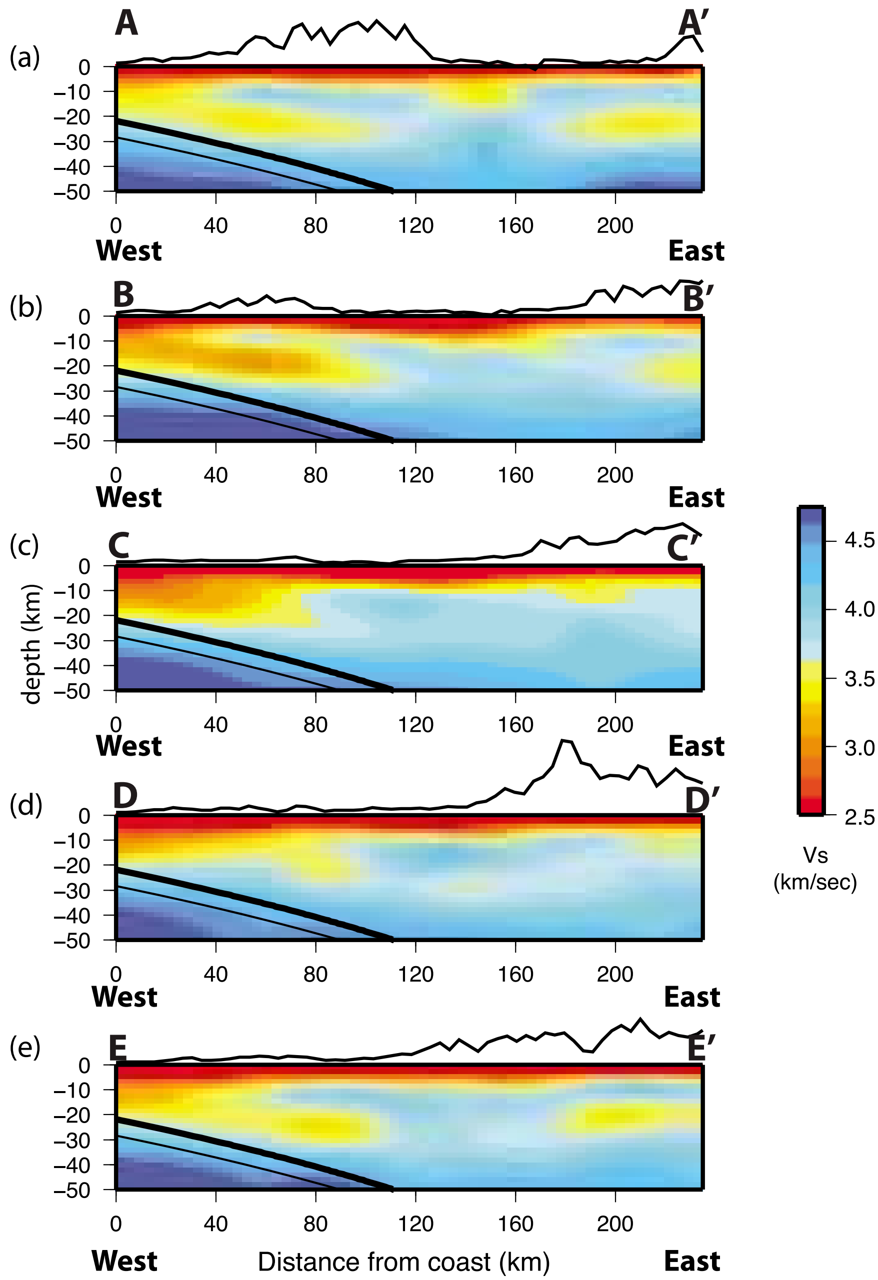

Figure 7. (a–e) West-east oriented cross sections through the final shear velocity model. Horizontal distance of 0 corresponds to the coastline. The east dipping heavy black line on the west of each section indicates the estimated location of the top of the slab inferred from scattered wave imaging [*Abers et al.*, 2009]. The thin black line mirrors the plate interface 7 km deeper to estimate the Moho of the subducting plate. Locations of the cross sections are indicated by black lines and labels on the map in Figure 6.

velocities along the east, and particularly southeast edge of the Olympic Peninsula at 0.18 Hz correlate well with geologic [e.g., *Tabor and Cady*, 1978] and previously recognized seismic signatures of the mafic Crescent terrane [e.g., *Tréhu et al.*, 1994; *Parsons et al.*, 1998]. The igneous core of the Cascades appears as a high phase velocity swath along the eastern edge of the array, particularly in the 0.18–0.09 Hz range. At longer periods (Figure 4d), the E-W gradient decreases as the high velocities of the Juan de Fuca slab begin to affect velocities near the coast. The overall dominance of low phase velocities along the margin results from the diffuse sensitivity of even 20–30 s Rayleigh waves to shear velocities over a broad vertical range, from mid-crustal to near Moho depths (Figure 4f).

4.2. Shear Velocity

[18] The shear velocity maps (Figure 5) and cross sections (Figures 6–7) are more easily interpreted in terms of regional geologic and tectonic features than are the phase velocity maps. The Vs structure is markedly different above the thrust zone, west of ~123°E, and beneath the arc, and we therefore discuss these two regions separately.

4.2.1. Structure Above and Below the Thrust Zone (West of 123°E)

[19] The near surface maps (Figures 5a and 5b) reveal low velocities (Vs < 2.4 km/s) in the Everett, Seattle, and Tacoma basins that flank the eastern and southern edges of Puget Sound, and the coastal Willapa-Grays Harbor basin. Seismic, gravity, and well data indicate that the coastal basins are approximately 5 km deep [*Parsons et al.*, 1998] while the Puget Sound area basins range from 6 to 9 km [*Brocher et al.*, 2001]. Low velocities along the margin continue to subbasin depths, however, and persist as an eastward dipping band of sharply reduced velocities (Vs = 3.0–3.3 km/s) to depths of 25 km beneath the Puget Lowlands (Figures 5c–5g and 6b). Aside from a narrow E-W striking band of higher midcrustal velocities (3.6–3.7 km/s) near 47°N (Figures 5f and 6b), the LVZ continues southward to the edge of the CAFE array near the Oregon-Washington border.

[20] The midcrustal LVZ extends beneath faster material in the shallow crust as it dips eastward, particularly beneath the Olympic peninsula, where velocities at 20 km are as low as 3.0 km/s (Figures 7a and 7b). This same pattern is also observed on the south end of the array, near cross section E-E′ (Figure 7e). Earlier tomographic models have imaged similar patterns in P wave velocity, and attribute the structure to underthrusting of accretionary wedge metasedimentary rocks beneath the Crescent terrane [*Parsons et al.*, 1999; *Ramachandran et al.*, 2006]. The faster rocks overlying the LVZ have shear velocities of 3.8–4.1 km/s, within the expected range of basalt and gabbro at midcrustal temperatures and pressures [*Hacker et al.*, 2003] and consistent with the interpretation that these high velocities are the subsurface expression of the oceanic affinity Crescent terrane [*Miller et al.*, 1997; *Ramachandran et al.*, 2006]. The slight convex eastward curvature (in map view) of these high velocity units near 47°N (Figure 5c) matches patterns observed in surface outcrops [*Schuster*, 2005].

[21] Beginning near depths of 25 km along the coastline and extending eastward with increasing depth, a distinct high velocity (Vs > 4.5 km/s) body is imaged. The depth and general location of this body (Figures 7a–7e) correlate well with the presumed location of the subducting Juan de Fuca slab based on local seismicity [*McCrory et al.*, 2004], refraction studies [*Parsons et al.*, 1998; *Preston et al.*, 2003], and migration images derived from converted body waves [*Abers et al.*, 2009]. High velocities are noticeably absent at the bottom (50 km) of north-south cross section G-G′ (Figure 6c), where the slab surface is expected to be near 80 km. Although the resolution of our tomography is insufficient to illuminate the details of the transition from lower continental crust to slab crust to slab upper mantle, shear velocities of 4.6 km/s at 50 km depth on the west end of the array are in good agreement with P wave tomographic results [e.g., *Preston et al.*, 2003; *Calvert et al.*, 2006] and within the range of expected values for anhydrous upper mantle peridotites [e.g., *Hacker et al.*, 2003].

4.2.2. Subarc Structure (East of 123°E)

[22] In contrast to the Juan de Fuca mantle farther west, velocities at mantle depths of 40–50 km beneath the arc are less than 4.2 km/s and do not exhibit a steep vertical gradient (Figure 6c). This region has been noted in several active source seismic studies [e.g., *Miller et al.*, 1997; *Snelson*, 2001] as a zone of weak or entirely absent Moho reflections. Receiver function studies from the very early [*Langston*, 1979] to recent [*MacKenzie*, 2008; *Nikulin et al.*, 2009] report difficulty in selecting an unambiguous Moho conversion between 15 and 50+ km depth, although several interfaces have been reported, and suggest the prevalence of dipping or highly anisotropic layers. Likewise, our results indicate unusual structures beneath the arc, with high velocity rocks in the 15–20 km depth range west and northwest of Mt. Rainier overlying slower material at 25–30 km (Figure 7d). To the south and east, layered structures are imaged at shallower depths (Figure 7e), however it is not clear whether these structures are contiguous with those to the north and west.

[23] The tectonic history of the Cascades region is complex, and thus there are several possible explanations for the layering and high velocities observed at midcrustal depths. High velocities might reflect the presence of the frozen residua of magmatic processes associated with the eastward migration of the Cascade volcanic arc since 35 Ma [*Priest*, 1990]. Previous studies [e.g., *Lees and Crosson*, 1990] have suggested that buried plutons are present west of Mt. Rainier, and simple mass and chemical balance dictate that fractionation of basaltic parent material within the crust necessarily creates a mafic to ultramafic residue that is complementary to the felsic/intermediate compositions emplaced at or near the surface [e.g., *Kay and Kay*, 1991, 1993; *Tatsumi et al.*, 2008]. An interpretation of a refraction line on the Columbia River Plateau [*Catchings and Mooney*, 1988] suggested that Eocene rifting might have caused interlayering of peridotites and basalt to depths as shallow as 25 km beneath south central Washington, and it is possible that these structures continue westward in some form beneath the eastern foothills of the Cascades.

[24] The transition from shear velocities typical of lower crustal materials to relatively low upper mantle velocities occurs near the bottom our model and is not resolved as a sharp discontinuity, unlike the Juan de Fuca Moho farther west. In the northeast corner of the study area, south and slightly west of Glacier Peak (Figure 6a), velocities at the bottom of the Vs model are near typical upper mantle values of 4.4–4.5 km/s at 45 km depth.

4.3. Vp/Vs Model

[25] To further constrain the various contributions of composition and fluids to the velocity structure, we quantitatively compare our results with the P wave velocity (Vp) compilation of R. Crosson (personal communication, 2010; for details on the Vp model, see http://earthweb.ess.washington.edu/lnk/crosson/INVER/index.html; a depth slice at 20 km through the Vp model is included as supplementary Figure 3, and a representative cross section is included in Figure 8a). The Vp/Vs ratio is directly related to Poisson's ratio [*Christensen*, 1996], making it useful in deriving petrologic inferences from seismic data. We interpolate the Vp model onto the same three-dimensional grid as our Vs estimate and divide the former by the latter. While the differences between the Vp and Vs models (in resolution, amplitude recovery, regularization parameters, gridding etc.) introduce some uncertainty and likely obscure small-scale variations, the overall patterns in Vp/Vs should be reliable in the central overlapping portions of the two grids.

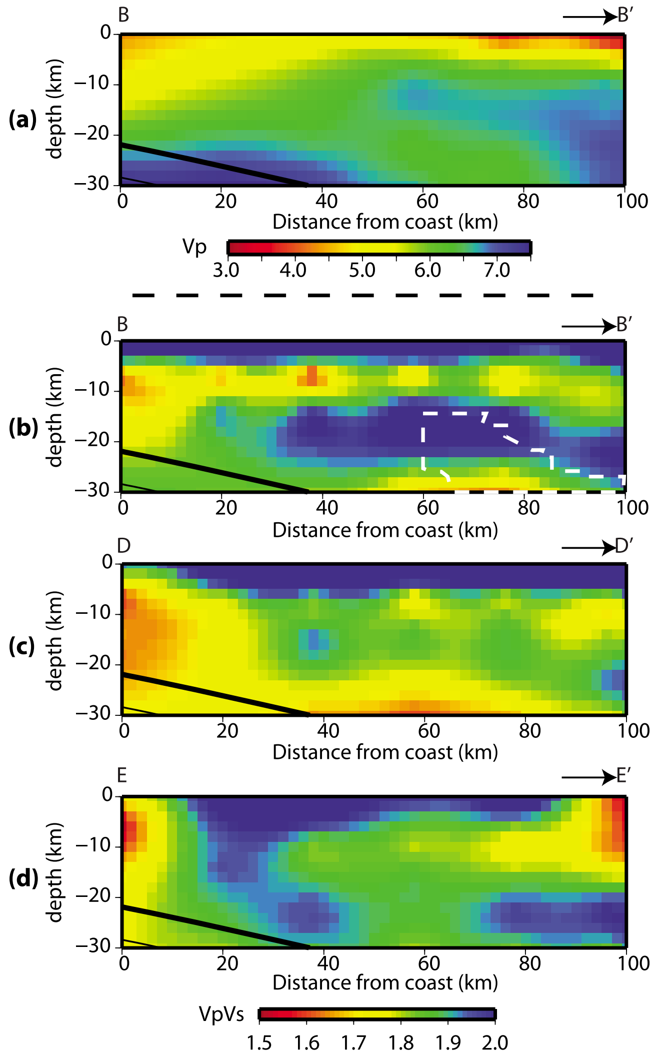

Figure 8. Vp/Vs calculated via comparing our Vs model with the Vp tomographic model of R. Crosson (personal communication, XXXX; http://earthweb.ess.washington.edu/lnk/crosson/INVER/index.html). (a) For reference, a Vp cross section along line B-B′ is plotted showing an eastward dipping zone of low Vp directly above the subducting slab, similar to the low-Vs tongue imaged in this work. (b–d) Vp/Vs cross sections correspond to the western portions of lines B-B′, D-D′, E-E′ in Figure 7. The white dashed line in Figure 8b shows the outline of the low-velocity body (Vp < 6.6 km/s) imaged by *Ramachandran et al.* [2006] along a nearly identical cross section.

[26] Assessing uncertainty in our Vp/Vs estimates is made difficult by the lack of published uncertainty analysis on the Vp measurements, as is the case with most body wave tomography studies, because of the lack of an explicit inverse operator and because of nonlinearities and underparameterization inherent in such inversions. As a substitute for direct measures of uncertainty in Vp, we compare velocities reported in several studies (R. Crosson, personal communication, XXXX) [*Ramachandran et al.*, 2006; *Preston*, 2003; *Parsons et al.*, 1999] at a depth of 20 km at the point 47.5°N, 123.5°W, and arrive at a conservative estimate of δVp = ±0.1 km/s based on the variation between these studies. While it is possible that the partially overlapping data sets used in creating the aforementioned Vp models would lead to some systematic bias in the results, the sheer volume of sources used (with additional earthquake and anthropogenic sources included in the later studies) and the variety of inversion techniques applied should conspire to reduce similarities in artifacts between the models. Using Vs values and formal uncertainties (~0.07 km/s) from our model (see section 5.3), we estimate 1-sigma uncertainty for Vp/Vs in the region of the midcrustal LVZ west of 123°W, where both data sets are densely sampled, to be 0.04.

[27] Under-recovery errors due to imperfect resolution in the Vp and Vs models could potentially increase the uncertainty. We expect this effect to be mitigated, however, based on the assumption that smoothing in both models would tend to make the sign (if not necessarily the amplitude) of under-recovery errors the same. Also, because the feature of most interest is a low-velocity midcrustal body, under-recovery would indicate that true velocities are even lower than the extremely low velocities already estimated. In particular, lower Vp/Vs than observed would require Vp less than the 6.0 km/s within the low-velocity body, even more difficult to reconcile with any anhydrous, low-porosity composition that would be consistent with low Vp/Vs ratios.

[28] Three vertical sections through the Vp/Vs grid are presented in Figure 8, corresponding to the western ends of lines B-B′, D-D′, and E-E′ in Figure 7. The most striking feature in the resulting model is the zone of high Vp/Vs (>1.9, corresponding to Poisson's ratio > 0.31) between 18 and 24 km beneath the Olympic peninsula and, to a lesser extent, near the latitude of Willapa Bay. This feature is notably absent, however, beneath line D-D′ along 47°N. In all of the Vp models we used for comparison, the high Vp/Vs anomaly is associated with a zone of low Vp (Figure 8, Figure S3 of the auxiliary material) within the resolution limits of the tomographic techniques.[1] The decrease in Vp is of smaller magnitude than the accompanying decrease in Vs, however, resulting in the Vp/Vs anomaly that clearly differs from the surrounding crust, where Vp/Vs is consistent with expected values for crustal rocks of ~1.75–1.82 [e.g., *Brocher and Christensen*, 2001].

5. Discussion

5.1. Horizontal Resolution

[29] In order to estimate the horizontal resolution of our inversion (step 2 of the processing), we performed a series of checkerboard tests (Figure 9) by tracing rays through an input grid with alternating high and low velocities, then inverting the resulting travel time measurements to produce phase velocity models. Random noise scaled to the uncertainty associated with each observation was added to the synthetic data before inversion. Damping was applied at the same level as that used to invert the data, and each synthetic travel time was weighted according to the uncertainty associated with the corresponding measurement in the observed data. Results are presented from synthetic travel time measurements using paths corresponding to observations in the 0.15 Hz data set, but tests run with only those

[1] Auxiliary materials are available in the HTML. doi:10.1029/2010JB007657.

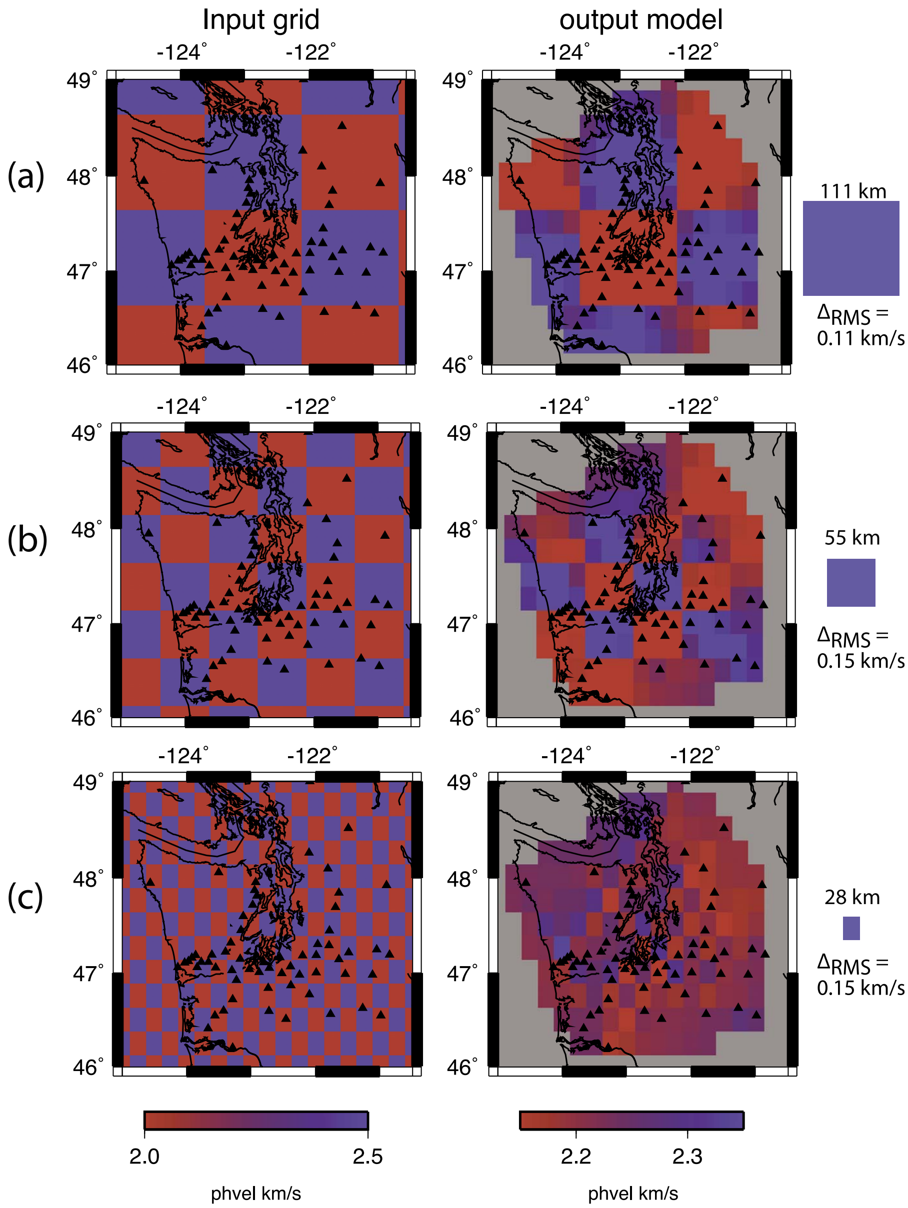

Figure 9. Checkerboard tests of horizontal resolution of the phase velocity tomography. (left) Input models consist of roughly square grids with block sizes of (a) 111 km, (b) 55 km, and (c) 28 km. (right) The results of processing synthetic travel time measurements through the input grid with inversion parameters identical to those applied to the data presented in Figure 4. The RMS difference between starting and ending models is shown to the right of each profile. Small triangles mark station locations.

paths measured at 0.03 Hz (the smallest data set) show nearly identical resolution.

[30] Results of tests using input grids measuring approximately 28 × 28 km, 55 × 55 km and 111 × 111 km are presented in Figure 9. Throughout the study area, phase velocity variations with length scales of 111 km are recovered extremely well (Figure 9a), with peak-to-peak variations nearly identical to the input model at the center of the uniform cells. Along cell margins and at the extremities of the array, velocities are smeared slightly due in part to the damping applied during the inversion. Peak to peak amplitude muting of less than 10% is observed. Tests using cells measuring 28 km on a side were also performed and suggest that there is considerable sensitivity to velocity variations at this length scale in the center of the array, but with more significant muting of amplitude variations (Figure 9c). The combined effects of adding noise to the synthetic data, smearing, and under-recovery result in RMS differences between the input and recovered models of 0.15 km/s for the 28 × 28 km and 55 × 55 km checkerboard tests, and 0.11 km/s for the 111 × 111 km square test.

[31] All analyses are performed assuming frequency-independent ray theory. Because of finite frequency effects, however, the true resolving power of our approach is probably somewhat less than that implied by Figure 9, particularly at the longer periods [e.g., *Yang and Forsyth*, 2006]. We conservatively estimate that along the E-W backbone of the array near 47°N, the data are sufficient to

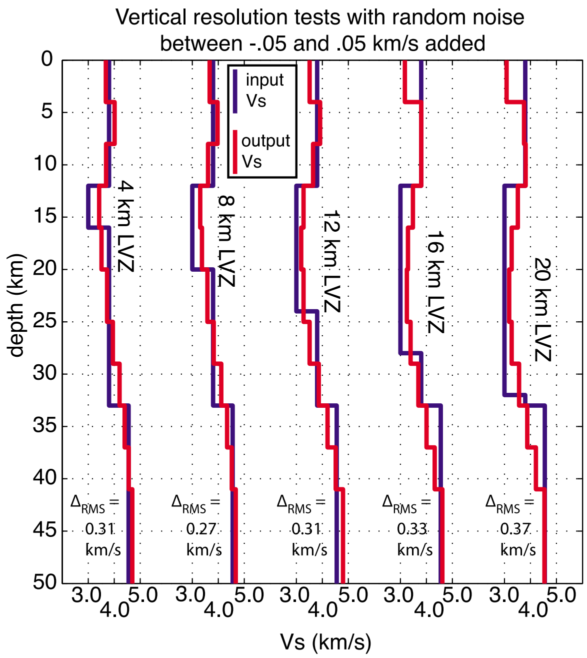

Figure 10. 1-D vertical recovery tests of the shear velocity inversion. From left to right, columns show input velocity structures and solutions for models with a midcrustal low-velocity zone increasing in thickness from 4 km to 20 km. The velocity decreases by 0.8 km/s in the midcrust and increases by 0.75 km/s at the Moho (33 km) in all models. Random noise between −0.05 and 0.05 km/s has been added to each of the synthetic phase velocity observations used in the inversion. Inversion parameters are identical to those applied to the data presented in Figure 5–7. The RMS difference between input and output models is shown at the bottom left of each profile.

resolve velocity variations in the mid to upper crust with a horizontal length scale on the order of 55 km with 95% amplitude recovery (Figure 9b). Figure 9c indicates that the best resolved portion of our model should also detect shallow velocity anomalies (where sensitivity is greatest at high frequencies) on length scales approaching the 0.25° grid spacing, albeit with a greater degree of under-recovery. In the lower crust, where Rayleigh wave sensitivity is peaked in the 20 s period range, resolution may degrade slightly due to the increasing width of the first Fresnel zone (~60–120 km for the paths used in this study), more so with increasing period [e.g., *Yoshizawa and Kennett*, 2002].

5.2. Vertical Resolution

[32] To test the vertical resolution of the phase-to-shear velocity inversion (step 3 of our processing), we performed synthetic tests using Vs models with midcrustal low-velocity zones (LVZs) of varying thickness. Random noise (−0.05 km/s < noise < 0.05 km/s) was added to each of the synthetic phase velocity observations before inverting for Vs, and the starting model and inversion parameters were identical to those used in processing data. Results (Figure 10) indicate that a midcrustal LVZ thicker than ~6 km is resolvable, and the amplitude of the velocity decrease is well resolved for LVZs thicker than ~8 km. Vertical smearing is more pronounced at the bottom of the LVZ than at the top, particularly when the bottom edge approaches the simulated Moho in the input model. Due to the combined effects of damping in the Vs inversion and double peaks in the Rayleigh wave sensitivity kernels at midcrustal and shallow depths (Figure 4f), large low-velocity zones in the middle crust tend to artificially introduce low-velocity features at the shallowest levels in the output models. These artifacts may result in underestimation of the shallow shear velocities in our model, but should have minimal impact on the mid to lower crustal velocities that are the primary focus of this study. Tests were also performed to investigate the possible introduction of low-velocity artifacts in the mid-crust due to mismapping of shallow low-velocity structures (e.g., sedimentary basins), and the adverse effects were found to be minimal. For realistic input models, with Vp and Vs decreased by 50% in a zone extending from the surface to 4 km depth, the output model shows a minor reduction of <1.8% in Vs between 17 and 25 km.

[33] Resolution tests using a starting model containing a low Vs subducting crust on top of the slab similar to that revealed by scattered wave migration (Figure 7b) [*Abers et al.*, 2009] show that the resolution of our ambient noise tomography (ANT) models is insufficient to image a thin (~5 km), dipping low-velocity zone in the 20–45 km depth range. This lack of very fine scale resolution is to be expected and emphasizes the complementary nature of the two techniques; scattered waves are sensitive to the short wavelength velocity discontinuity structure but can be relatively blind to high amplitude changes in velocity that are spread over broad spatial dimensions. The test also emphasizes that our data and methodology tend to vertically smear sharp discontinuities in velocity and likely obscure the fine-scale velocity structure at the top of the Juan de Fuca plate, but are sensitive to the first-order crust-mantle transition here.

[34] Comparison of results obtained from inversions with and without the additional long period observations from *Yang et al.* [2008] show improved resolution of structures below ~40 km, but very little difference at shallower levels. Notably, Vs models resulting from inversions of the ambient noise data alone still show the subducting slab near the coastline beneath the center of the array (Figure S1).

5.3. Uncertainty Analysis

[35] Due to the difficulty in calculating meaningful formal uncertainty estimates through two stages of weighted and smoothed inversions by linearized error propagation, we assess the uncertainty in our phase and shear velocity estimates via bootstrap analysis [*Efron and Gong*, 1983]. We produced 1000 bootstrap sets from the full set of interstation phase velocity observations, randomly resampling with replacement the individual phase velocity measurements, and processed each set through the phase velocity regularization and shear velocity inversion procedures detailed above. Thus, the bootstrap analysis propagates errors through both the two-dimensional inversions for phase velocity and the vertical inversion for Vs. Because we have only the final phase velocity model for the ballistic data provided by *Yang et al.* [2008] rather than the raw, path-averaged phase velocity observations, we fixed the 40, 50, and 66 s phase velocities at each grid point in all of our

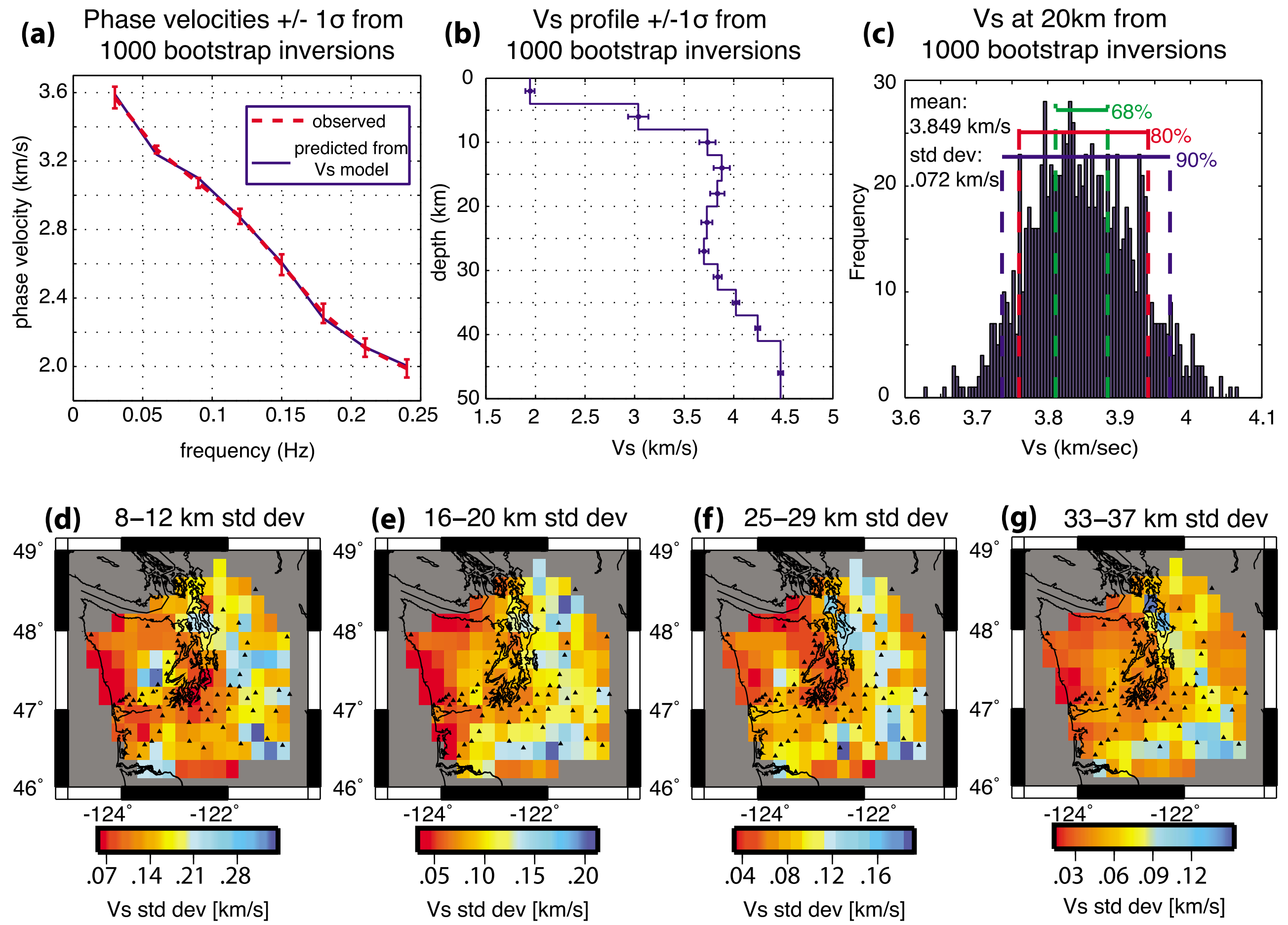

Figure 11. Uncertainty in phase and shear velocity estimates from 1000 bootstrap-resampled data sets. (a–c) Results from one representative grid point near the center of the study area (47.125, −122.875). The red dashed line in Figure 11a is the dispersion curve from the final model with 1σ error bounds from bootstrap analysis. For comparison, the dispersion curve (blue solid line) predicted by the 1-D shear velocity profile (Figure 11b) at the same grid point is also shown in Figure 11a. Histogram in Figure 11c shows the distribution of all bootstrap velocity estimates at the same grid node with green, red, and blue dashed lines denoting the bounds that contain 68%, 80%, and 90% of the shear velocity solutions, respectively. (d–g) Plots show 1-sigma uncertainty of shear velocity estimates at selected depths in the final model.

bootstrap sets. All inversion parameters were set to the same values applied to the full data set, and uncertainty is reported as the standard deviation of all 1000 phase and shear velocity estimates at each grid point, which should give an unbiased estimate of measurement uncertainty provided the individual phase velocity measurements are independent and similarly distributed [*Efron and Gong*, 1983].

[36] Histograms of bootstrap results at each grid node (Figure 11) tend to have near-normal distributions that cluster around the mean value with few extreme outliers. An example from one grid point near the middle of the array is presented in Figure 11e, and is representative of the observed distributions of bootstrap Vs estimates throughout the study area. We estimate 1-sigma uncertainties of 70–150 m/s for our mid to lower crustal shear velocities within the CAFE array (Figures 11a–11d), with the higher values generally occurring east of ~122°. The apparent decrease in uncertainty with increasing depth is likely a result of the stabilizing effect of the fixed long-period phase velocities in the bootstrap sets rather than an indication that our deeper Vs estimates are more precise. As *Yang et al.* [2008] report very small uncertainties (10–15 m/s in phase velocity), the expected slight variations in these long period data should have negligible effects on the Vs model between the surface and 50 km depth (see sensitivity kernels in Figure 4f). In areas of sparser ray coverage, such as the northwest corner of the study area (Figure 11), estimating the standard deviation via bootstrap analysis appears to give unrealistically small uncertainties, perhaps because a small number of stations sample all paths there and the assumption of uncorrelated errors is not correct.

5.4. Frequency Domain NCF Analysis and Path Length Limitations

[37] One of the benefits of extracting phase velocities directly from the spectral NCF is that we are able to obtain

reliable measurements for stations separated by sub-wavelength distances [*Ekström et al.*, 2009]. The first zero crossing of J_0 is approximately

$$z_1 \approx 0.38 \times 2\pi \tag{3}$$

Combining equations (2) and (3), the theoretical minimum interstation distance is then

$$r_{\min} = \frac{\lambda_n z_1}{2\pi} \approx 0.38\lambda_n \tag{4}$$

where λ_n is the wavelength corresponding to the frequency of interest, ω_n.

[38] If attainable, this is a marked improvement over most previous studies using time domain NCF's, which implicitly interpret the NCF using the far-field approximation of the Green's function [e.g., *Yao et al.*, 2006] and therefore require minimum station spacing of 2–3 times the wavelength of interest [e.g., *Lin et al.*, 2007]. Including the station pair paths with lengths between 0.38λ and 3λ allows us to increase the total number of observations by greater than 58% and increase resolution. As the maximum dimension of our array is ~250 km, the 3λ limitation would preclude the use of any data with periods longer than ~24 s, and would cut the number of useable paths at 17 s by more than 75%. As a result, when the data set is limited to paths longer than 3λ, results degrade so as to show no hint of the subducting slab in cross section.

[39] The effect of the 3λ limitation on two interstation paths is illustrated in Figures 3c–3f, where we plot the number of cycles n of a Rayleigh wave with frequency f traveling at reference velocity c that would fit between the two stations ($n = f * r/c$, or $n = r/\lambda$) on the upper horizontal axis. The red vertical dashed line represents the usual three-cycle limit. The real parts of the spectra (black lines in Figures 3c and 3d), however, appear to be well-behaved functions (i.e., oscillatory and quasiperiodic without any drastic swings in amplitude) down to frequencies as low as 0.05 Hz.

[40] We investigate the reliability of estimating phase velocities along short paths by comparing results at a single frequency (0.09 Hz) from five subsets of the full data set segregated by path length (Figure 12). Only those stations within 20 km of the centerline of the main E-W swath of the array are included in this analysis (Figure 12a). Each subset is limited to interstation paths within a specified range of length, expressed as the ratio of interstation distance to wavelength (r/λ), or number of cycles (n). A simple one-dimensional regularization of the phase velocities from each subset reveals that interstation paths as short as 0.5–1 wavelength (blue lines and symbols in Figures 12b–12d) recover consistent velocities; they show the same general patterns of phase velocities as subsets containing longer paths and the full data set (Figure 12c). For reasons that are still unclear, however, paths shorter than 1λ show higher scatter at frequencies below 0.09 Hz than they do at higher frequencies (Figures 12e–12f). As a test to ensure that the increased scatter associated with short paths does not introduce a systematic bias, we performed a second, full inversion using only paths longer than 3λ. The resulting Vs model (Figure S2) shows the same features as the preferred model presented herein, with only slight differences in resolution, blurring some features near the edges of prominent anomalies. We therefore conclude that our approach yields reliable phase velocity measurements between stations separated by as little as 1 wavelength (potentially less), and the addition of the shorter paths increases both resolution and spatial coverage dramatically (Figure 12d).

[41] Average phase velocity measurements from the spectral NCFs decrease monotonically as a function of frequency (Figure 4e) and are similar, on average, to those reported in other surface wave studies of the western United States [e.g., *Lin et al.*, 2008]. Our Vs models are also in qualitatively good agreement with several P wave tomographic studies of the same region (comparing Figure 5 with the works of *Parsons et al.* [1999], *Preston et al.* [2003], and *Ramachandran et al.* [2006]). These correlations, in conjunction with the excellent match between phase velocity maps of the Western U.S. from spectral NCFs [*Ekström et al.*, 2009] and those obtained from traditional ANT [*Lin et al.*, 2008], give us confidence that the spectral NCF method is a reliable means of measuring surface wave velocities to path lengths as small as 0.5–1 wavelength.

6. Conclusions

6.1. Low Vs, High Vp/Vs Anomaly in Western Washington

[42] Very low shear velocities in conjunction with Poisson's ratios in excess of 0.30 are rare for rocks typical of the continental crust, with notable exceptions being highly porous rocks [*Hyndman*, 1988], serpentinite, and anorthosite [*Christensen*, 1996]. The presence of large bodies of either serpentinite or anorthosite seems unlikely; there are no known occurrences of significant amounts of anorthosite associated with the Cascadia subduction zone, and serpentine, while common in hydrated ultramafic rocks, is a relatively minor constituent of altered gabbros. Very high concentrations of chlorite would also drastically reduce Vs and increase Vp/Vs, but a rock would have to be nearly 100% chlorite to reduce shear velocities to 3.3 km/s at midcrustal pressures [*Christensen*, 2004]. Furthermore, very high abundances of chlorite are unlikely in the lower continental crust.

[43] Considering instead alteration products that would be expected in the mafic-to-intermediate rocks likely to make up the overriding plate in the Cascadia forearc, chlorite is predicted at significantly lower concentrations. For example, if the bulk composition is gabbroic, at pressures of <1 GPa and temperatures ranging from 200 to 500°C, the mid to lower crust should be in the blueschist/greenshist or prehnite-pumpellyite metamorphic facies [*Hacker et al.*, 2003, Figures 1 and 6]. Chlorite is present in these rocks at no more than ~20% abundances. The major H_2O carriers (lawsonite, epidote, prehnite, pumpellyite) are not slow enough to explain the depressed velocities we observe, having shear velocities in the range of 4–5 km/s.

[44] Using the method of *Hacker and Abers* [2004], seismic properties were calculated at 1 GPa and 400°C for the compositions (prehnite-pumpellyite facies, pumpellyite-actinolite facies, greenschist facies, and lawsonite blueschist facies) that are likely in the lower crust of the overriding

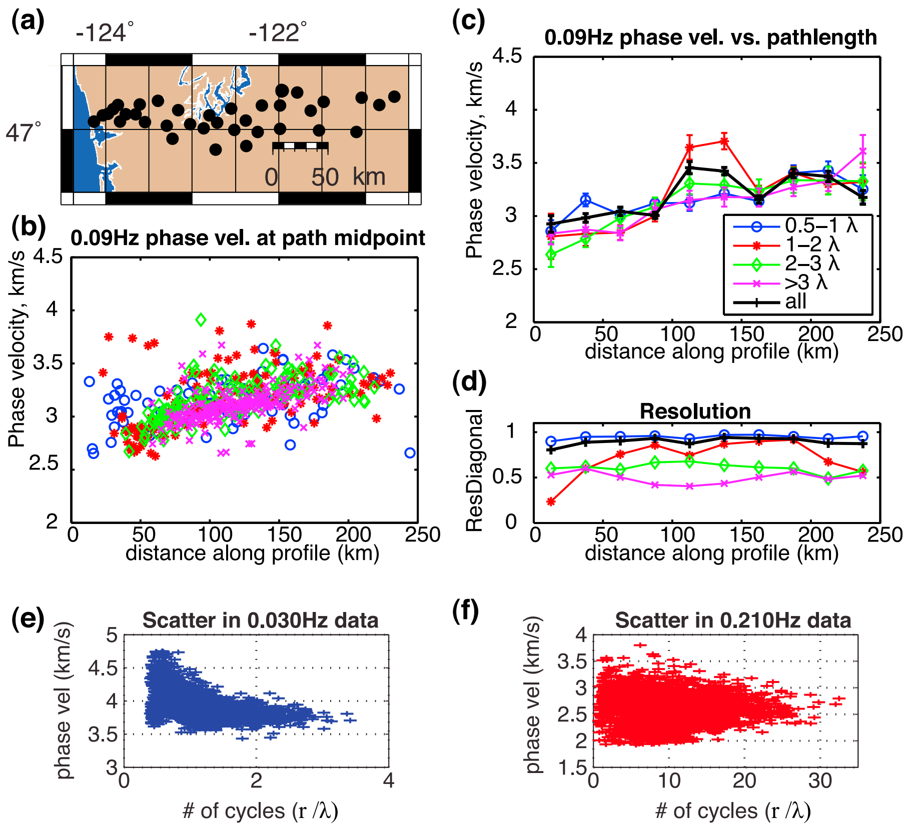

Figure 12. Plots illustrating the relationship between phase velocity and interstation distance. Paths were grouped based on the ratio r/λ (interstation distance/wavelength at 0.09 Hz or, equivalently, number of cycles). Colors and symbols in Figures 12b–12d correspond to subsets with r/λ ratios in the ranges indicated by the legend in Figure 12c. (a) Map shows stations that were included in the analysis. (b) Individual phase velocity estimates are plotted at path midpoints. (c) Phase velocity profiles resulting from a 1-D regularization using each of the subsets, and (d) the corresponding resolution diagonals. Note that the overall pattern of increasing velocity from west to east is clear for all subsets, and resolution improves significantly with the addition of shorter paths. (e and f) Scatter in phase velocity observations as a function of path length for the 0.03 Hz and 0.21 Hz observations, respectively. The increased scatter at short offsets in the 0.03 Hz data is the subject of ongoing investigation.

plate at a subduction zone [*Hacker et al.*, 2003]. Vs ranges from 3.89–4.10 km/s, and Vp/Vs ranges from 1.76–1.81. Vs are still too high and Vp/Vs are still low to explain the observations with these hydrated mafic low-P compositions. Other lithologies with high mica contents might be expected to have lower Vs, but it is very hard to explain Vs as low as 3.0 km/s and Vp/Vs as high as 1.9 with just the solid mineralogies expected for altered mafic rock.

[45] We therefore conclude that the low Vs, high Vp/Vs signature is likely due to a highly porous, fluid-rich lower crust, and potentially high pore fluid pressures [*Audet et al.*, 2009; *Takei*, 2002, *Christensen*, 1984]. High fluid pressures at the plate interface have been inferred based on extremely high Vp/Vs ratios beneath Washington [*Abers et al.*, 2009] and Vancouver Island [*Audet et al.*, 2009] measured from receiver functions. Our results suggest that similar fluid porosities exist shallower, in the overriding plate. The Vp/Vs ratios we observe within the lower crust are lower than some estimates inferred directly at the plate interface, but they are consistent with receiver function modeling estimates at the same depths from the CAFE array [*Abers et al.*, 2009].

6.2. Structure of the Overriding Crust

[46] The shallow shear velocity structure beneath western Washington is highly heterogeneous on length scales of 25 km or less (Figures 5–7). Within ~100 km of the coast, the slab is clearly imaged as a high-Vs (>4.5 km/s), east dipping body. Above the slab, a distinct low-Vs tabular anomaly dominates the image, with velocities <3.1 km/s observed as deep as 20 km. These low velocities and associated high Vp/Vs ratios likely stem from a highly porous, fluid-rich lower crust resulting from either accretion of saturated sediments or dewatering of the subducting slab. As suggested by *Hyndman* [1988] in his analysis of the highly reflective lower crust beneath Vancouver Island, fluids from a dehydrating slab provide a ready source for saturating the lower crust as they percolate upward through the overlying plate over the long history of subduction beneath northwestern North America (Figure 13). We cannot rule out underthrusting of saturated accretionary wedge material as the source of fluids, however, and this interpretation has been favored by *Ramachandran et al.* [2006]

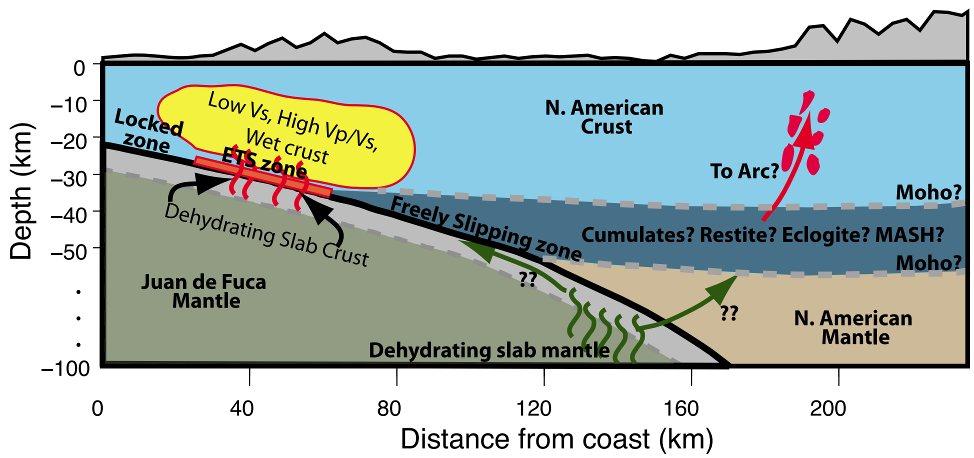

Figure 13. Cartoon illustrating the main features of the Vs model near the center of the CAFE array and possible interpretations.

to explain the coincident zone of low P wave velocities in the Olympic Peninsula.

[47] The low Vs anomaly is absent, however, near 47°N, suggesting a change in lithology or fluid saturation state. This change in velocity structure could be due to either preexisting variations in crustal architecture or to variations in the amount of fluid percolating upward from the plate interface. South of ~47°N, the overriding plate transitions from Olympic Complex accretionary wedge material to accreted terranes of oceanic affinity [e.g., *Parsons et al.*, 1999; *Brandon et al.*, 1998], which might be expected to correspond to a decrease in crustal porosity and permeability. The high velocities associated with the slab surface also appear to be slightly deeper (Figure 6b) at the same latitude, however. Also, previous workers have noted distinct changes in slab morphology and/or dynamics based on teleseismic arrivals [e.g., *Michaelson and Weaver*, 1986] and a lack of intraslab earthquakes [*McCrory et al.*, 2004], implying a change in conditions within the slab. Thus, the LVZ may vary either because of changes in overriding plate composition or in the abundance of fluids derived from the downgoing plate.

6.3. Relevance to ETS and Earthquakes

[48] It has been suggested that the density, rheology, and fluid content of the overriding plate control the occurrence of ETS [e.g., *Brudzinski and Allen*, 2007]. In western Washington, however, patterns in shear velocity structure in the overriding plate appear to be vertically coincident with changes in structure or morphology of the subducting slab and velocities just below the plate interface [*Abers et al.*, 2009], suggesting a linkage across the plate boundary that is hard to explain solely in terms of overriding plate influence. The prominent midcrustal LVZ beneath the Olympic peninsula collocates, in map view, with a very active zone of tremor activity and episodic slip (ETS) that occurs on a fairly regular 14 ± 2 month cycle [e.g., *Rogers and Dragert*, 2003; *Wech and Creager*, 2008; *Ghosh et al.*, 2009] (Figure 14). The vertical correlation of the two features is less clear, however, given the debate over whether the tremor occurs within the crust [e.g., *Kao et al.*, 2005] or at the plate interface [*Brown et al.*, 2009; *La Rocca et al.*, 2009]. Very few regular (i.e., impulsive, high frequency) earthquakes occur along the thrust zone in this region [e.g., *Taber and Smith*, 1985; *Preston et al.*, 2003], but earthquakes within the slab are observed [*McCrory et al.*, 2004] and often presumed to be associated with dehydration embrittlement [e.g., *Preston et al.*, 2003].

[49] ETS is segmented along strike, as evinced by patches with distinct initiation and termination points common to repeating episodes, and varying recurrence intervals between those patches [*Brudzinski and Allen*, 2007; *Boyarko et al.*, 2009]. Both intraslab seismicity and the 14 month ETS patch seem to terminate, or at least attenuate markedly, southward near 47°N. Comparison of ETS locations with geodetic transients, overriding plate topography, and major subducting plate asperities led *Brudzinski and Allen* [2007] to propose a boundary between distinct ETS zones with different recurrence intervals at the same latitude. While some tremor is detected at individual seismic stations south of this line [*Wech and Creager*, 2009; *Brudzinski and Allen*, 2007], the tremor appears to be less abundant and to recur at different intervals farther south [*Boyarko et al.*, 2009]. The observations presented in this paper also indicate a sharp division in the shear velocity structure of the overriding plate and in the upper portion of the Juan de Fuca slab at 47°N. The existence of a major tectonic boundary at 47°N has been widely recognized, and variously attributed to changes in accreted terrane lithology [*Brudzinski and Allen*, 2007], along-strike variations in mantle geochemistry [*Schmidt et al.*, 2008], or a gap in the Juan de Fuca slab [*Porritt et al.*, 2009].

[50] The change in crustal velocity structure coincident with drastic changes in intermediate-depth earthquakes and tremor-related seismicity suggests some form of common origin for these phenomena across the plate boundary. The fact that the shear velocity structure in both the overriding and subducting plates appears to change at the same latitude near the coastline, where the incoming slab has been in contact with the weak accretionary wedge for only ~3 Ma, suggests that the overriding plate is not driving the linked evolution of the two plates. Furthermore, it is difficult to

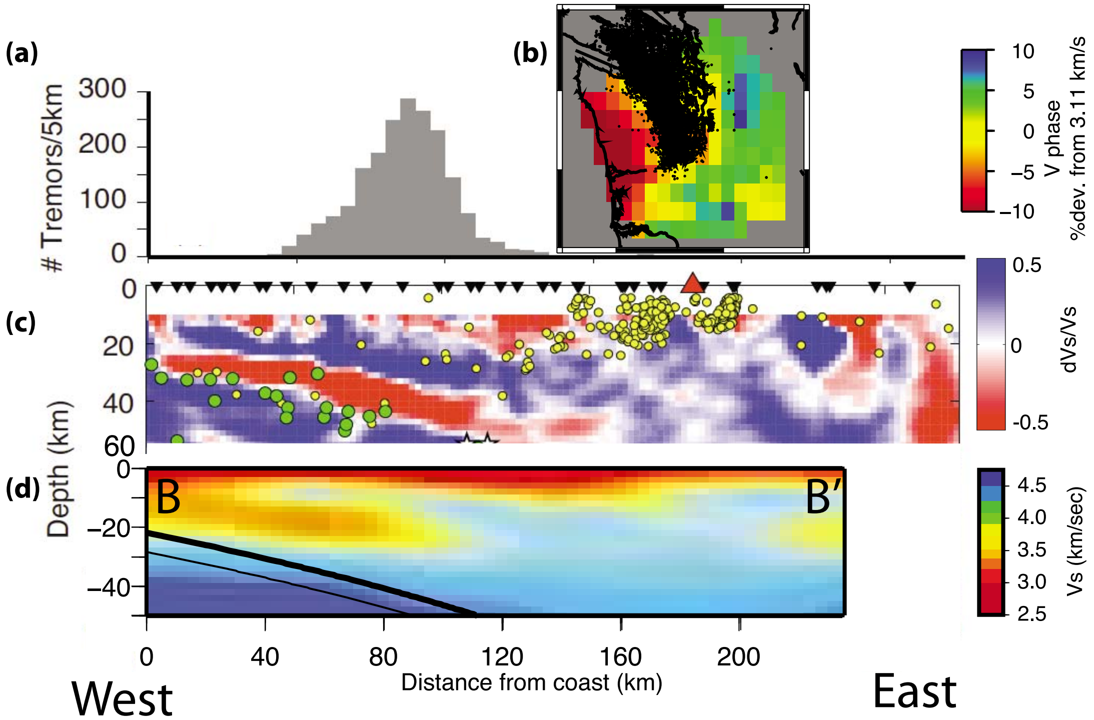

Figure 14. Comparison of ambient noise tomography with migration imaging and episodic tremor and slip (ETS) locations. (a) Histogram and (b) black dots superimposed on the 0.09 Hz phase velocity map indicate tremor locations during the 2004, 2005, 2007, and 2008 ETS events [*Wech and Creager*, 2008]. (c) Migration image of *Abers et al.* [2009, Figure 2], along the CAFE E-W transect at 47°N, with background colors corresponding to Vs gradients. Yellow and green circles indicate crustal and slab earthquakes, respectively, the former from the catalog of *McCrory et al.* [2004] and the latter recorded during the CAFE deployment; the red triangle indicates the location of Mt. Rainier. (d) Shear velocity cross section is line B-B′ from Figure 7. Horizontal and vertical scales are the same in Figures 14c and 14d.

envision the crustal LVZ impacting the occurrence of intraslab earthquakes. It seems likely, therefore, that some persistent feature on the Juan de Fuca plate intersects the plate margin near 47°N and at least partially controls the frictional behavior of the plate interface and the shear velocity structure of the overriding North American Plate.

[51] High pore fluid pressures are thought to be necessary to allow slow slip at a subduction interface [*Kodaira et al.*, 2004]. Multichannel seismic observations of the Juan de Fuca plate indicate a highly variable hydration pattern in the crust, with extensive crustal-scale faults developing away from the ridge and possibly creating fluid conduits into the upper mantle [*Nedimovic et al.*, 2009]. If these hydration patterns are long-lived and intersect the trench at relatively fixed positions over geologic time, prolonged fluid flux across the plate boundary could be expected to effectively lubricate the plate interface and hydrate and weaken the overriding plate. The orientation of pseudofaults, parallel to plate motion, suggests that downgoing plate segmentation has indeed had a roughly constant geometry with respect to the North American plate [*Nedimovic et al.*, 2009]. Therefore, we hypothesize that a significant and long-lived along-strike change in the fluid content of the slab may occur near 47°N that, possibly in combination with changes in accreted terrane lithology, controls or modulates overriding plate hydration and ETS in Western Washington. Perhaps this change imposes a barrier to interplate rupture propagation across ~47°N, potentially limiting the size of megathrust earthquakes beneath the continental margin. Alternatively, changes in subducting plate curvature may be responsible for the segmentation, as suggested by recent fault slip models based on GPS records of slow slip events [*Schmidt and Gao*, 2010].

6.4. Summary

[52] Our results provide the first high-resolution model of shear velocity structure beneath Western Washington (compare with the recent results of *Yang et al.* [2008] and *Moschetti et al.* [2010]; see also Figure S4), revealing a highly heterogeneous overriding plate and a low Vs, high Vp/Vs lower crust beneath western Washington. An E-W oriented boundary near 47°N appears to separate distinct structural zones in both the overriding and subducting plates and to demarcate a change in ETS behavior at the plate interface, perhaps indicating persistent spatial patterns in the hydration state of the subducting slab.

[53] This study also further demonstrates the utility of the spectral ambient noise correlation technique introduced by *Ekström et al.* [2009]. The technique is capable of measuring phase velocities between stations separated by distances equal to, and possibly less than, the wavelength of surface waves at the frequency of interest. This is a significant

improvement over ambient noise studies using time domain NCFs and group velocities. Spectral ambient noise tomography, therefore, has the potential to greatly enhance the resolution of shear velocity measurements beneath dense seismic arrays, and to allow for phase velocity estimation at longer periods where path lengths are limited by geography.

[54] **Acknowledgments.** The authors would like to thank Josh Stachnik and Aaron Ferris for sharing their algorithm for calculating noise correlation functions, Spahr Webb for suggesting the approach to measuring phase velocities, Yingjie Yang for sharing his long period phase velocity data, and Bob Crosson for his Vp grid of Western Washington. CAFE is an EarthScope Flexible Array program, supported by the IRIS PASSCAL Instrument Center. We thank the large group of volunteers who participated in CAFE operations. This work funded by the National Science Foundation grant EAR-0544847. Figures were prepared using the GMT programs [*Wessel and Smith*, 1991].

References

Abers, G. A., L. S. Mackenzie, S. Rondenay, Z. Zhang, A. G. Wech, and K. C. Creager (2009), Imaging the source region of Cascadia tremor and intermediated-depth earthquakes, *Geology*, *37*, 1119–1122, doi:10.1130/G30143A.1.

Abramowitz, M., and I. Stegun (Eds.) (1965), *Handbook of Mathematical Functions, With Formulas, Graphs, and Mathematical Tables*, Dover, Mineola, N. Y.

Aki, K. (1957), Space and time spectra of stationary waves with special reference to microtremors, *Bull. Earthquake Res. Inst. Univ. Tokyo*, *25*, 415–456.

Atwater, B. F. (1987), Evidence for great Holocene earthquakes along the outer coast of Washington State, *Science*, *236*, 942–944.

Atwater, B. F. (1992), Geologic evidence for earthquakes during the past 2000 years along the Copalis River, southern coastal Washington, *J. Geophys. Res.*, *97*, 1901–1919, doi:10.1029/91JB02346.

Audet, P., M. G. Bostock, N. I. Christensin, and S. M. Peacock (2009), Seismic evidence for overpressured subducted oceanic crust and megathrust fault sealing, *Nature*, *457*, 76–78, doi:10.1038/nature07650.

Bensen, G. D., M. H. Ritzwoller, M. P. Barmin, A. L. Levshin, F. Lin, M. P. Moschetti, N. M. Shapiro, and Y. Yang (2007), Processing seismic ambient noise data to obtain reliable broad-band surface wave dispersion measurements, *Geophys. J. Int.*, *169*, 1239–1260, doi:10.1111/j.1365-246X.2007.03374.x.

Boyarko, D. C., M. R. Brudzinski, R. M. Allen, and R. W. Porritt (2009), Non-volcanic tremor in Cascadia: Segmented along strike, anti-corrrelated with earthquakes, and offset from the locked zone, *Eos Trans. AGU*, *90*(52), Fall Meet. Suppl., Abstract T11C–1827.

Brandon, M. T., M. K. Roden-Tice, and J. I. Garver (1998), Late Cenozoic exhumation of the Cascadia accretionary wedge in the Olympic Mountains, northwest Washington state, *Geol. Soc. Am. Bull.*, *110*, 985–1009, doi:10.1130/0016-7606(1998)110<0985:LCEOTC>2.3.CO;2.

Brocher, T. M., and N. I. Christensen (2001), Density and velocity relationships for digital sonic and density logs from coastal Washington and laboratory measurements of Olympic peninsula mafic rocks and greywackes, *U.S. Geol. Surv. Open File Rep.*, 01–264, 30 pp.

Brocher, T. M., T. Parsons, R. J. Blakely, N. I. Christensen, M. A. Fisher, and R. E. Wells, and SHIPS Working Group (2001), Upper crustal structure in Puget Lowland, Washington: Results from the Seismic Hazards Investigation in Puget Sound, *J. Geophys. Res.*, *106*, 13,541–13,564, doi:10.1029/2001JB000154.

Brown, J. R., G. C. Beroza, S. Ide, K. Ohta, D. R. Shelly, S. Y. Schwartz, W. Rabbel, M. Thorwart, and H. Kao (2009), Deep low-frequency earthquakes in tremor localize to the plate interface in multiple subduction zones, *Geophys. Res. Lett.*, *36*, L19306, doi:10.1029/2009GL040027.

Brudzinski, M. R., and R. M. Allen (2007), Segmentation in episodic tremor and slip all along Cascadia, *Geology*, *35*, 907–910, doi:10.1130/G23740A.1.

Bustin, A., R. D. Hyndman, A. Lambert, J. Ristau, J. He, H. Dragert, and M. Van der Kooij (2004), Fault parameters of the Nisqually earthquake determined from moment tensor solutions and the surface deformation form GPS and InSAR, *Bull. Seismol. Soc. Am.*, *94*(2), 363–376, doi:10.1785/0120030073.

Calvert, A. J., K. Ramachandran, H. Kao, and M. A. Fisher (2006), Local thickening of the Cascadia forearc crust and the origin of seismic reflectors in the uppermost mantle, *Tectonophysics*, *420*, 175–188, doi:10.1016/j.tecto.2006.01.021.

Catchings, R. D., and W. D. Mooney (1988), Crustal structure of the Columbia Plateau: Evidence for continental rifting, *J. Geophys. Res.*, *93*, 459–474, doi:10.1029/JB093iB01p00459.

Christensen, N. I. (1984), Pore pressure and oceanic crustal seismic structure, *Geophys. J. R. Astron. Soc.*, *79*, 411–423.

Christensen, N. I. (1996), Poisson's ratio and crustal seismology, *J. Geophys. Res.*, *101*, 3139–3156, doi:10.1029/95JB03446.

Christensen, N. I. (2004), Serpentinites, peridotites, and seismology, *Int. Geol. Rev.*, *46*(9), 795–816, doi:10.2747/0020-6814.46.9.795.

Cox, H. (1973), Spatial correlation in arbitrary noise fields with applications to ambient sea noise, *J. Acoust. Soc. Am.*, *54*, 1289–1301, doi:10.1121/1.1914426.

DeMets, C., and T. H. Dixon (1999), New kinematic models for Pacific–North America motion from 3 Ma to present: 1. Evidence for steady motions and biases in the NUVEL-1A model, *Geophys. Res. Lett.*, *26*(13), 1921–1924, doi:10.1029/1999GL900405.

DeShon, H. R., S. Y. Schwartz, S. L. Bilek, L. M. Dorman, V. Gonzalez, J. M. Protti, E. R. Flueh, and T. H. Dixon (2003), Seismogenic zone structure of the southern Middle America Trench, Costa Rica, *J. Geophys. Res.*, *108*(B10), 2491, doi:10.1029/2002JB002294.

Dragert, H., K. Wang, and G. Rogers (2004), Geodetic and seismic signatures of episodic tremor and slip in the northern Cascadia subduction zone, *Earth Planets Space*, *56*, 1143–1150.

Efron, B., and G. Gong (1983), A leisurely look at the bootstrap, the jackknife, and cross-validation, *Am. Stat.*, *37*(1), 36–48, doi:10.2307/2685844.

Ekström, G., G. A. Abers, and S. C. Webb (2009), Determination of surface-wave phase velocities across USArray from noise and Aki's spectral formulation, *Geophys. Res. Lett.*, *36*, L18301, doi:10.1029/2009GL039131.

Fuller, C. W., S. D. Willett, and M. T. Brandon (2006), Formation of forearc basins and their influence on subduction zone earthquakes, *Geology*, *34*, 65–68, doi:10.1130/G21828.1.

Ghosh, A., J. E. Vidale, J. R. Sweet, K. C. Creager, and A. G. Wech (2009), Tremor patches in Cascadia revealed by seismic array analysis, *Geophys. Res. Lett.*, *36*, L17316, doi:10.1029/2009GL039080.

Goldfinger, C., C. H. Nelson, and J. E. Johnson (2003), Holocene earthquake records from the Cascadia subduction zone and northern San Andreas Fault based on precise dating of offshore turbidites, *Annu. Rev. Earth Planet. Sci.*, *31*, 555–577, doi:10.1146/annurev.earth.31.100901.141246.

Hacker, B. R., and G. A. Abers (2004), Subduction factory: 3. An Excel worksheet and macro for calculating the densities, seismic wave speeds, and H_2O contents of minerals and rocks at pressure and temperature, *Geochem. Geophys. Geosyst.*, *5*, Q01005, doi:10.1029/2003GC000614.

Hacker, B. R., G. A. Abers, and S. M. Peacock (2003), Subduction factory: 1. Theoretical mineralogy, densities, seismic wave speeds, and H_2O contents, *J. Geophys. Res.*, *108*(B1), 2029, doi:10.1029/2001JB001127.

Harmon, N., D. Foryth, and S. Webb (2007), Using ambient seismic noise to determine short-period phase velocities and shallow shear velocities in young oceanic lithosphere, *Bull. Seismol. Soc. Am.*, *97*(6), 2009–2023, doi:10.1785/0120070050.

Harmon, N., P. Gerstoft, C. A. Rychert, G. A. Abers, M. S. de la Cruz, and K. M. Fischer (2008), Phase velocities from seismic noise using beamforming and cross correlation in Costa Rica and Nicaragua, *Geophys. Res. Lett.*, *35*, L19303, doi:10.1029/2008GL035387.

Herrmann, R. B., and C. J. Ammon (2004), *Computer Programs in Seismology: Surface Waves, Receiver Functions, and Crustal Structure*, St. Louis Univ., St. Louis, Mo.

Hyndman, R. D. (1988), Dipping seismic reflectors, electrically conductive zones, and trapped water in the crust over a subducting plate, *J. Geophys. Res.*, *93*, 13,391–13,405, doi:10.1029/JB093iB11p13391.

Hyndman, R. D., and K. Wang (1995), The rupture zone of Cascadia great earthquakes from current deformation and the thermal regime, *J. Geophys. Res.*, *100*, 22,133–22,154, doi:10.1029/95JB01970.

Jordan, T. E., B. L. Isacks, R. W. Allmendinger, J. A. Brewer, V. A. Ramos, and C. J. Ando (1983), Andean tectonics related to geometry of subducted Nazca plate, *Geol. Soc. Am. Bull.*, *94*(3), 341–361, doi:10.1130/0016-7606(1983)94<341:ATRTGO>2.0.CO;2.

Kao, H., S.-J. Shan, H. Dragert, G. Rogers, J. F. Cassidy, and K. Ramachandran (2005), A wide depth distribution of seismic tremors along the northern Cascadia margin, *Nature*, *436*, 841–844, doi:10.1038/nature03903.

Kao, H., S.-J. Shan, H. Dragert, and G. Rogers (2009), Northern Cascadia episodic tremor and slip: A decade of tremor observations from 1997 to 2007, *J. Geophys. Res.*, *114*, B00A12, doi:10.1029/2008JB006046.

Kay, R. W., and S. M. Kay (1991), Creation and destruction of lower continental crust, *Geol. Rundsch.*, *80*, 259–278, doi:10.1007/BF01829365.

Kay, R. W., and S. M. Kay (1993), Delamination and delamination magmatism, *Tectonophysics*, *219*, 177–189, doi:10.1016/0040-1951(93)90295-U.

Kelleher, J., and W. McCann (1976), Buoyant zones, great earthquakes, and unstable boundaries of subduction, *J. Geophys. Res.*, *81*, 4885–4896, doi:10.1029/JB081i026p04885.
Kodaira, S., T. Iidaka, A. Kato, J. O. Park, T. Iwasaki, and Y. Kaneda (2004), High pore fluid pressure may cause silent slip in the Nankai Trough, *Science*, *304*, 1295–1298, doi:10.1126/science.1096535.
Langston, C. A. (1979), Structure under Mount Rainier, Washington, inferred from teleseismic body waves, *J. Geophys. Res.*, *84*, 4749–4762.
La Rocca, M., K. C. Creager, D. Galluzzo, S. Malone, J. E. Vidale, J. R. Sweet, and A. G. Wech (2009), Cascadia tremor located near plat interface constrained by *S* minus *P* wave times, *Science*, *323*, 620–623, doi:10.1126/science.1167112.
Larson, A. M., J. A. Snoke, and D. E. James (2006), *S*-wave velocity structure, mantle xenoliths and the upper mantle beneath the Kaapvaal craton, *Geophys. J. Int.*, *167*, 171–186, doi:10.1111/j.1365-246X.2006.03005.x.
Lees, J. M., and R. S. Crosson (1990), Tomographic imaging of local earthquake delay times for three-dimensional velocity variation in western Washington, *J. Geophys. Res.*, *95*, 4763–4776, doi:10.1029/JB095iB04p04763.
Lin, F.-C., M. H. Ritzwoller, J. Townend, M. Savage, and S. Bannister (2007), Ambient noise Rayleigh wave tomography of New Zealand, *Geophys. J. Int.*, *170*, 649–666, doi:10.1111/j.1365-246X.2007.03414.x.
Lin, F.-C., M. P. Moschetti, and M. H. Ritzwoller (2008), Surface wave tomography of the western United States from ambient seismic noise: Rayleigh and Love wave phase velocity maps, *Geophys. J. Int.*, *173*, 281–298, doi:10.1111/j.1365-246X.2008.03720.x.
Liu, Y., and J. R. Rice (2007), Spontaneous and triggered aseismic deformation transients in a subduction fault model, *J. Geophys. Res.*, *112*, B09404, doi:10.1029/2007JB004930.
Ludwin, R. S., C. S. Weaver, and R. S. Crosson (1991), Seismicity of Washington and Oregon, in *Neotectonics of North America*, edited by D. B. Slemmons et al., pp. 77–98, *Geol. Soc. Am.*, Denver.
MacKenzie, L. S. (2008) A receiver function study of the Central America and Cascadia subduction zones, Ph.D. thesis, Boston Univ., Boston, Mass.
Madsen, J. K., D. J. Thorkelson, R. M. Friedman, and D. D. Marshall (2006), Cenozoic to recent plate configurations in the Pacific Basin: Ridge subduction and slab window magmatism in western North America, *Geosphere*, *2*, 11–34, doi:10.1130/GES00020.1.
McCaffrey, R. (2009), Time-dependent inversion of three-component continuous GPS for steady and transient source in northern Cascadia, *Geophys. Res. Lett.*, *36*, L07304, doi:10.1029/2008GL036784.
McCausland, W., S. Malone, and D. Johnson (2005), Temporal and spatial occurrence of deep non-volcanic tremor: From Washington to northern California, *Geophys. Res. Lett.*, *32*, L24311, doi:10.1029/2005GL024349.
McCrory, P. A., J. L. Blair, D. H. Oppenheimer, and S. R. Walter (2004), Depth to the Juan De Fuca slab beneath the Cascadia subduction margin: A 3-D model for sorting earthquakes, *U.S. Geol. Surv. Data Ser.*, *91*. (Available at http://pubs.usgs.gov/ds/91/)
Michaelson, C. A., and C. S. Weaver (1986), Upper mantle structure from teleseismic P wave arrivals in Washington and northern Oregon, *J. Geophys. Res.*, *91*, 2077–2094.
Miller, K. M., G. R. Keller, and J. M. Gridley (1997), Crustal structure along the west flank of the Cascades, western Washington, *J. Geophys. Res.*, *102*, 17,857–17,873, doi:10.1029/97JB00882.
Miller, M. M., T. Melbourne, D. J. Johnson, and W. Q. Sumner (2002), Periodic slow earthquakes from the Cascadia Subduction Zone, *Science*, *295*, 2423, doi:10.1126/science.1071193.
Moran, S. C., J. M. Lees, and S. D. Malone (1999), P wave crustal velocity structure in the greater Mount Rainier area from local earthquake tomography, *J. Geophys. Res.*, *104*, 10,775–10,786, doi:10.1029/1999JB900036.
Moschetti, M. P., M. H. Ritzwoller, and N. M. Shapiro (2007), Surface wave tomography of the western United States from ambient seismic noise: Rayleigh wave group velocity maps, *Geochem. Geophys. Geosyst.*, *8*, Q08010, doi:10.1029/2007GC001655.
Moschetti, M. P., M. H. Ritzwoller, F.-C. Lin, and Y. Yang (2010), Crustal shear wave velocity structure of the western United States inferred from ambient seismic noise and earthquake data, *J. Geophys. Res.*, *115*, B10306, doi:10.1029/2010JB007448.
Nedimovic, M. R., D. R. Bohnenstiehl, S. M. Carbotte, J. P. Canales, and R. P. Dziak (2009), Faulting and hydration of the Juan de Fuca plate system, *Earth Planet. Sci. Lett.*, *284*, doi:10.1016/j.epsl.2009.04.013.
Nicholson, T., M. Bostock, and J. F. Cassidy (2005), New constraints on subduction zone structure in northern Cascadia, *Geophys. J. Int.*, *161*, 849–859, doi:10.1111/j.1365-246X.2005.02605.x.
Nikulin, A., V. Levin, and J. Park (2009), Receiver funcion study of the Cascadia megathrust: Evidence for localized serpentinization, *Geochem. Geophys. Geosyst.*, *10*, Q07004, doi:10.1029/2009GC002376.
Parsons, T., A. M. Tréhu, J. H. Leutgert, K. Miller, F. Kilbride, R. E. Wells, M. A. Fisher, E. Flueh, U. S. ten Brink, and N. I. Christensen (1998), A new view into the Cascadia subduction zone and volcanic arc: Implications for earthquake hazards along the Washington margin, *Geology*, *26*, 199–202, doi:10.1130/0091-7613(1998)026<0199:ANVITC>2.3.CO;2.
Parsons, T., R. E. Wells, M. A. Fisher, E. Flueh, and U. S. ten Brink (1999), Three-dimensional velocity structure of Siletzia and other accreted terranes in the Cascadia forearc of Washington, *J. Geophys. Res.*, *104*, 18,015–18,039, doi:10.1029/1999JB900106.
Porritt, R. W., et al. (2009), Segmentation of the Cascades volcanic arc revealed through ambient noise based surface wave tomography, *Eos Trans. AGU*, *90*(52), Fall Meet. Suppl., Abstract V41B–2178.
Preston, L. A. (2003), Simultaneous inversion of 3D velocity structure, hypocenter locations, and reflector geometry in Cascadia, Ph.D. thesis, 135 pp., Univ. of Wash., Seattle.
Preston, L. A., K. C. Creager, R. S. Crosson, T. M. Brocher, and A. M. Tréhu (2003), Intraslab earthquakes: Dehydration of the Cascadia slab, *Science*, *302*, 1197–1200, doi:10.1126/science.1090751.
Priest, G. R. (1990), Volcanic and tectonic evolution of the Cascade volcanic arc, central Oregon, *J. Geophys. Res.*, *95*, 19,583–19,599, doi:10.1029/JB095iB12p19583.
Ramachandran, K., R. D. Hyndman, and T. M. Brocher (2006), Regional *P* wave velocity structure of the Northern Cascadia Subduction Zone, *J. Geophys. Res.*, *111*, B12301, doi:10.1029/2005JB004108.
Rogers, G., and H. Dragert (2003), Episodic tremor and slip on the Cascadia Subduction Zone: The chatter of silent slip, *Science*, *324*, 1025–1026, doi:10.1126/science.1084783.
Rondenay, S., M. G. Bostock, and J. Shragge (2001), Multiparameter two-dimensional inversion of scattered teleseismic body waves: 3. Application to the Cascadia 1993 data set, *J. Geophys. Res.*, *106*, 30,795–30,808.
Sabra, K. G., P. Gerstoft, P. Roux, and W. A. Kuperman (2005), Extracting time-domain Green's function estimates from ambient seismic noise, *Geophys. Res. Lett.*, *32*, L03310, doi:10.1029/2004GL021862.
Sanchez-Sesma, F., and M. Campillo (2006), Retrieval of the Green's function from cross correlation: The canonical elastic problem, *Bull. Seismol. Soc. Am.*, *96*(3), 1182–1191, doi:10.1785/0120050181.
Satake, K., K. Wang, and B. F. Atwater (2003), Fault slip and seismic moment of the 1700 Cascadia earthquake inferred from Japanese tsunami descriptions, *J. Geophys. Res.*, *108*(B11), 2535, doi:10.1029/2003JB002521.
Schmidt, D. A., and H. Gao (2010), Source parameters and time-dependent slip distributions of slow slip events on the Cascadia subduction zone from 1998 to 2008, *J. Geophys. Res.*, *115*, B00A18, doi:10.1029/2008JB006045.
Schmidt, M. E., A. L. Grunder, and M. C. Rowe (2008), Segmentation of the Cascadia Arc as indicated by Sr and Nd isotopic variation among diverse primitive basalts, *Earth Planet. Sci. Lett.*, *266*, 166–181, doi:10.1016/j.epsl.2007.11.013.
Schuster, E. J. (2005), Geologic map of Washington State, *GM-53*, Wash. Div. of Geol. and Earth Resour., Olympia.
Shapiro, N. M., and M. Campillo (2004), Emergence of broadband Rayleigh waves from correlations of the ambient seismic noise, *Geophys. Res. Lett.*, *31*, L07614, doi:10.1029/2004GL019491.
Shapiro, N. M., M. Campillo, L. Stehly, and M. H. Ritzwoller (2005), High-resolution surface-wave tomography from ambient seismic noise, *Science*, *307*, 1615–1618, doi:10.1126/science.1108339.
Snelson, C. M. (2001), Investigating crustal structure in western Washington and in the Rocky Mountains: Implications for seismic hazards and crustal growth, Ph.D. thesis, Univ. of Tex. at El Paso, El Paso.
Stachnik, J. C., K. Dueker, D. L. Schutt, and H. Yuan (2008), Imaging Yellowstone plume-lithosphere interactions from inversion of ballistic and diffusive Rayleigh wave dispersion and crustal thickness data, *Geochem. Geophys. Geosyst.*, *9*, Q06004, doi:10.1029/2008GC001992.
Taber, J. J., and S. W. Smith (1985), Seismicity and focal mechanisms associated with the subduction of the Juan de Fuca plate beneath the Olympic Peninsula, Washington, *Bull. Seismol. Soc. Am.*, *75*(1), 237–249.
Tabor, R. W., and W. M. Cady (1978) Geologic map of the Olympic Peninsula, Washington, *U.S. Geol. Surv. Misc. Invest. Map*, *I-994*.
Takei, Y. (2002), Effect of pore geometry on Vp/Vs: From equilibrium geometry to crack, *J. Geophys. Res.*, *107*(B2), 2043, doi:10.1029/2001JB000522.
Tatsumi, Y., H. Shukuno, K. Tani, N. Takahashi, S. Kodaira, and T. Kogiso (2008), Structure and growth of the Izu-Bonin-Mariana arc crust: 2. Role of crust-mantle ransformation and the transparent Moho in arc crust evolution, *J. Geophys. Res.*, *113*, B02203, doi:10.1029/2007JB005121.
Tréhu, A. M., I. Asudeh, T. M. Brocher, J. H. Luetgert, W. D. Mooney, H. L. Nabelek, and Y. Nakamura (1994), Crustal architecture of the

Cascadia forearc, *Science*, *266*, 237–243, doi:10.1126/science.266.5183.237.

Tréhu, A. M., J. Braunmiller, and J. L. Nabelek (2008), Probably low-angle thrust earthquakes on the Juan de Fuca-North America plate boundary, *Geology*, *36*, 127–130, doi:10.1130/G24145A.1.

Van Wagoner, T. M., R. S. Crosson, K. C. Creager, G. Medema, L. Preston, N. P. Symons, and T. M. Brocher (2002), Crustal structure and relocated earthquakes in the Puget Lowland, Washington, from high-resolution seismic tomography, *J. Geophys. Res.*, *107*(B12), 2381, doi:10.1029/2001JB000710.

Warren, L. M., J. A. Snoke, and D. E. James (2008), S-wave velocity structure beneath the High Lava Plains, Oregon, from Rayleigh-wave dispersion inversion, *Earth Planet. Sci. Lett.*, *274*, 121–131, doi:10.1016/j.epsl.2008.07.014.

Webb, S. C. (1986), Coherent pressure fluctuations observed at two sites on the deep sea floor, *Geophys. Res. Lett.*, *13*(2), 141–144, doi:10.1029/GL013i002p00141.

Wech, A. G., and K. C. Creager (2008), Automated detection and location of Cascadia tremor, *Geophys. Res. Lett.*, *35*, L20302, doi:10.1029/2008GL035458.

Wech, A. G., and K. C. Creager (2009), Cascadia-wide tremor locations, *Eos Trans. AGU*, *90*(52), Fall Meet. Suppl., Abstract T11C–1822.

Wech, A. G., K. C. Creager, and T. I. Melbourne (2010), Seismic and geodetic constraints on Cascadia slow slip, *J. Geophys. Res.*, *114*, B10316, doi:10.1029/2008JB006090.

Wells, R. E., R. J. Blakely, Y. Sugiyama, D. W. Scholl, and P. A. Dinterman (2003), Basin-centered asperities in great subduction zone earthquakes: A link between slip, subsidence, and subduction erosion?, *J. Geophys. Res.*, *108*(B10), 2507, doi:10.1029/2002JB002072.

Wessel, P., and W. H. F. Smith (1991), Free software helps map and display data, *Eos Trans. AGU*, *72*, 441–446, doi:10.1029/90EO00319.

Wilson, D. S. (2002) The Juan de Fuca plate and slab: Isochron structure and Cenozoic plate motions, *Rep. 02–238*, pp. 9–12, U.S. Geol. Surv., Reston, Va.

Yang, Y., and D. W. Forsyth (2006), Regional tomographic inversion of the amplitude and phase of Rayleigh waves with 2-D sensitivity kernels, *Geophys. J. Int.*, *166*, 1148–1160, doi:10.1111/j.1365-246X.2006.02972.x.

Yang, Y., M. H. Ritzwoller, F.-C. Lin, M. P. Moschetti, and N. M. Shapiro (2008), Structure of the crust and uppermost mantle beneath the western United States revealed by ambient noise and earthquake tomography, *J. Geophys. Res.*, *113*, B12310, doi:10.1029/2008JB005833.

Yao, H., R. D. van der Hilst, and M. V. de Hoop (2006), Surface-wave array tomography in SE Tibet from ambient seismic noise and two-station analysis—I. Phase velocity maps, *Geophys. J. Int.*, *166*, 732–744, doi:10.1111/j.1365-246X.2006.03028.x.

Yoshizawa, K., and B. L. N. Kennett (2002), Determination of the influence zone for surface wave paths, *Geophys. J. Int.*, *149*, 440–453, doi:10.1046/j.1365-246X.2002.01659.x.

G. A. Abers, J. A. Calkins, and G. Ekström, Lamont-Doherty Earth Observatory, Earth Institute at Columbia University, 61 Route 9w, Palisades, NY 10964, USA. (jcalkins@ldeo.columbia.edu)

K. C. Creager, Department of Earth and Space Science, University of Washington, Seattle, WA 98195, USA.

S. Rondenay, Department of Earth, Atmospheric, and Planetary Sciences, Massachusetts Institute of Technology, Cambridge, MA 02139, USA.